The effect of muscovite on the microstructural evolution and rheology of quartzite in general shear

L. Tokle [a,b,d,*], G. Hirth [b], H. Stünitz [c,d]

[a] *Structural Geology and Tectonics Group, Geological Institute, Department of Earth Sciences, ETH Zürich, Sonneggstrasse 5, 8092, Zürich, Switzerland*
[b] *Department of Earth, Environmental and Planetary Sciences, Brown University, Providence, RI, 02912, USA*
[c] *Institut des Sciences de la Terre d'Orléans (ISTO), UMR 7327, 1A, Rue de la Ferollerie, Université d'Orléans, 45100, Orléans, France*
[d] *Department of Geosciences, University of Tromsø, 9037, Tromsø, Norway*

ABSTRACT

We conducted general shear experiments on synthetic mixtures of quartz and muscovite aggregates at 800 °C and 1.5 GPa with 0.1 wt% H_2O added in the Griggs apparatus to investigate the role of muscovite content on the microstructural evolution and rheological properties of quartz aggregates. Muscovite content varied between 0, 5, 10 and 25% muscovite. Mechanically, the sample strengths decrease with an increase in muscovite content. At high strains muscovite grains align sub-parallel to the shear plane with C′- bands commonly observed in the muscovite-bearing samples. The presence of muscovite has significant influence on the amount of dynamic recrystallization in quartz; at high strains the pure quartz sample completely recrystallizes while only ~5% of the quartz in the 25% muscovite sample is dynamically recrystallized at similar strains. The presence of muscovite also has a significant influence on crystallographic preferred orientations (CPO) and grain shape preferred orientations (SPO) of quartz at high strains. At high strains, muscovite is interpreted to deform primarily by basal glide and dissolution-precipitation creep. Finally, our mechanical results fit well with rheological mixing models, where we estimate aggregates with 25% muscovite may deform 1–2 orders of magnitude faster than pure quartz aggregates at conditions near the brittle-ductile transition.

1. Introduction

Micas are a ubiquitous accessory phase found throughout the continental crust; however, the quantitative effects of micas on the ductile strength of the continental crust are poorly constrained. Thus, rheologic models for the continental crust are typically based on single phase flow laws for quartz and/or feldspar. Deformation experiments on mica single crystals show that micas are weak relative to quartz, with a highly nonlinear rheology; micas deform primarily by kinking and slip along their basal plane (e.g., Bell et al., 1986; Meike 1989; Kronenberg et al., 1990; Mares and Kronenberg, 1993). In addition, deformation experiments on fine-grained muscovite aggregates show a Newtonian rheology (Mariani et al., 2006). Naturally deformed mica shows evidence for a range of deformation processes, including basal slip, kinking, and diffusion creep (Bell et al., 1986; Bell and Cuff 1989; Hippertt 1994; Mulch et al., 2006), and exhibit a newly described type of defect termed "ripplocations" (Aslin et al., 2019), making the characterization of plastic deformation in micas complex.

In this study, we investigate the influence of muscovite on the strength of quartz aggregates. The aggregate strength, or aggregate rheology, depends on the phase abundance, phase distribution, phase strength contrast, and the active deformation mechanisms in each phase, all of which can change with variations in pressure, temperature, stress, strain rate, and increasing strain (Handy 1990, 1994, Holyoke and Tullis, 2006). Rheological mixing models have been developed to quantify the aggregate viscosity of two-phase materials by utilizing end-member flow laws for the different materials (e.g., Tullis et al., 1991; Huet et al., 2014; Rast and Ruh, 2021).

The role of micas on polyphase aggregate rheology has been investigated in several experimental studies, including work on quartz–muscovite aggregates (Tullis and Wenk, 1994), biotite-rich gneiss (Holyoke and Tullis, 2006a;b), and mica–quartz/feldspar aggregates (Gottschalk et al., 1990; Shea and Kronenberg, 1992, 1993; Rawling et al., 2002). Of these studies, only Holyoke and Tullis (2006aa,b) and

---

* Corresponding author. Structural Geology and Tectonics Group, Geological Institute, Department of Earth Sciences, ETH Zürich, Sonneggstrasse 5, 8092, Zürich, Switzerland.

E-mail address: leif.tokle@erdw.ethz.ch (L. Tokle).

Tullis and Wenk (1994) performed experiments at conditions where quartz deforms by dislocation creep. Tullis and Wenk (1994) deformed synthetically mixed powders of quartz and muscovite in axial compression with a volume percent of muscovite ranging from 0 to 100%. Strong crystallographic preferred orientations (CPO) of muscovite grains show alignment of the basal plane perpendicular to the σ_1 direction. This orientation is not favorable for glide and thus does not illustrate the role of muscovite on weakening in shear zones. Holyoke and Tullis (2006a, 2006b) conducted general shear experiments on gneiss, investigating the phase strength contrast (PSC) between quartz, feldspar, and biotite and how the PSC affected strain localization and the mechanisms by which strain localization initiates. Holyoke and Tullis (2006a) concluded that stress concentrations at the tips of biotite grains promoted interconnection of weak layers with increasing strain. As a consequence of using a natural rock, Holyoke and Tullis (2006a, b) performed experiments at a single volume percent of mica (~13%).

A potential consequence of the high temperatures that are necessary to experimentally deform quartz at dislocation creep conditions is that muscovite and biotite can breakdown at these temperatures through the loss of hydroxyls, referred to as dehydroxylation, resulting in either the neocrystallization of new phases or partial melting (Guggenheim et al., 1987; Rubie and Brearley, 1987; Brearley and Rubie, 1990; Mazzucato et al., 1999; Mariani et al., 2006). This has limited most deformation experiments at low confining pressures on muscovite and biotite to T ≤ 400 °C (Kronenberg et al., 1990; Shea and Kronenberg, 1992, 1993; Mares and Kronenberg, 1993). Low pressure shear experiments conducted by Mariani et al. (2006), show that samples with high pore-fluid pressure can inhibit muscovite breakdown at temperatures up to 700 °C. While at high pressures, ≥1.0 GPa, and high temperatures, ≥700 °C, it has been shown that the kinetics for breakdown in micas are slow relative to the timescales of rock deformation experiments (Rubie and Brearley, 1987; Brearley and Rubie, 1990) and that both muscovite and biotite are largely stable over the time scale of experimental studies (e.g. ≤100 h) with only minor amounts of breakdown products observed in select regions in only a few samples of quartz-muscovite aggregates (Tullis and Wenk, 1994) and pure biotite aggregates (Holyoke and Tullis, 2006a, 2006b, 2006c). The one example of a dehydration reaction in mica-bearing aggregates at high temperatures and high pressures are the deformation experiments conducted by Holyoke and Tullis (2006c) of Gneiss Minuti; however, the dehydration reaction was a result of the polyphase starting material and deformation conditions and not the stability of biotite.

We designed a series of deformation experiments in the Griggs apparatus to investigate the role of muscovite content on quartz rheology and microstructural evolution. Care was taken to avoid significant chemical breakdown of muscovite in order to study only mechanical effects of mixing quartz and mica. We conducted general shear experiments to low and high strains on synthetically prepared quartz aggregates with 0–25 vol% muscovite to explore how the presence of muscovite influences a) dynamic recrystallization in quartz; b) the evolution of quartz crystallographic preferred orientations (CPO) and grain shape preferred orientations (SPO) with increasing strain; c) strain localization in a quartz-rich rock; and d) the effective viscosity of a muscovite-bearing quartzite.

2. Experimental methods

2.1. Starting material

Samples were prepared by mixing powders derived from Black Hills Quartzite (BHQ) and Black Hills Muscovite (BHM), the same materials used by Tullis and Wenk (1994). The BHQ powder was sieved to a grain size of 63–100 μm while the BHM powder was sieved to a grain size of 45–73 μm. Powders were prepared with 0, 5, 10, and 25% muscovite by volume. Quartz and muscovite powders were first mixed together in an acetone slurry in a glass beaker. The beaker was placed in an ultrasonic

bath and the slurry was mixed until the acetone completely evaporated and no visible clumps remained (e.g. de Ronde et al., 2005). This procedure mitigates grain size and density sorting, as well as mineral segregation.

2.2. Experimental procedures

The sample assembly and deformation geometry are shown in Fig. 1. Alumina shear pistons were cut at 45° to each other to produce an inclined-piston shear geometry. The shear pistons were jacketed in a Pt sleeve with Ni foil inserted between the alumina shear pistons and the Pt jacket. The starting material powder is placed between the two shear pistons with 0.1 wt% water added, and the assembly is weld-sealed using Pt cups at the ends of the shear pistons. As is true for all undrained experiments, the exact pH₂O and potential for gradients within the sample is not measured; however, the lack of significant variation in microstructure within each sample (section 3.2), indicates uniform pH₂O at the sample-scale. For comparison with previous work, we calculate water fugacity assuming that pH₂O is equal to the confining pressure. NaCl is used as the confining medium. All deformation experiments were conducted at 800 °C, 1.5 ± 0.1 GPa confining pressure, and a shear strain rate ~1.6–3.2 × 10⁻⁵ s⁻¹.

Three types of experiments were conducted on each of the prepared starting powders: hydrostatic annealing for 34 h, high strain ($\gamma \approx 4.0$) experiments that achieved nominally steady state flow, and low strain experiments that were quenched when samples reached peak stress ($\gamma \approx 0.6$). To preserve the microstructures, at the end of each experiment the temperature was lowered at a rate of 4 °C/s to 200 °C. The confining pressure decreased by ~250 MPa during the initial temperature drop and was subsequently lowered to room pressure and temperature while maintaining a modest differential stress to suppress decompression cracking.

2.3. Image analysis

After experiments, samples were impregnated in epoxy and standard petrographic thin sections were prepared perpendicular to the shear plane, parallel to the shear directions, and polished to first-order grey colors for quartz. Photomicrographs were taken with circular polarized and crossed polarized light for microstructural analysis. Circular polarized light micrographs were used to analyze grain size, SPO, CPO, and sample-scale phase maps. Cross-polarized light and back-scatter electron (BSE) images were used to examine deformation microstructures. 2D Phase maps were created in ImageJ to estimate the volume percent of each phase as well as the amount of quartz dynamic recrystallization by comparing the phase maps of relict grains and dynamically recrystallized grains. The term "relict" quartz grain is used for grains that are interpreted to remain largely unrecrystallized and typically have a grain size ≥50 μm.

SPOs were analyzed using grain boundary maps of relict quartz grains. We used the SURFOR (SURFace ORientation) method in 5-degree increments to quantify the surface fabric of the grain boundary maps in relation to the shape, size, and orientation of the two-dimensional surfaces relative to the deformation geometry (Panozzo, 1984). The orientation of the long axis of grains is displayed in length-weighted rose diagrams, where the average length of each 5-degree increment is normalized by the maximum average length whereas the average grain shape is represented by the long particle axis (b-axis) and the short particle axis (a-axis). The aspect ratio of the average grain shape is determined by taking the long particle axis divided by the short particle axis for each grain boundary map.

Crystallographic preferred orientations (CPOs) were measured using computer-integrated polarized (CIP) microscopy (Panozzo Heilbronner and Pauli, 1993; Heilbronner and Tullis, 2006). CIP maps are constructed from the central region of each sample, where strain is most uniform. Quartz CPOs were derived from the freeware Image SXM
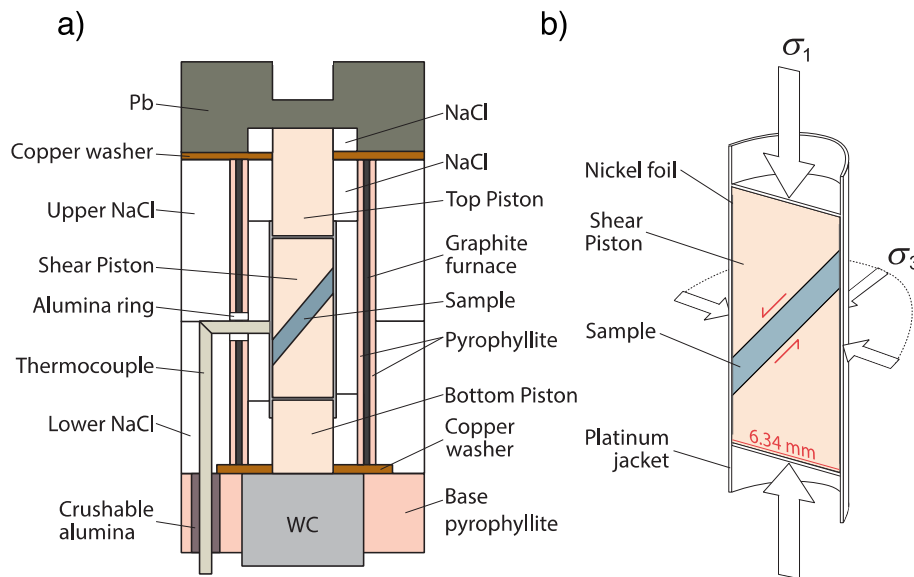
a)

b)

Fig. 1. Illustration of the all-salt assembly and general shear sample for the Griggs apparatus. a) cross-sectional view of the sample assembly. b) 3D cross-sectional view perpendicular to the shear plane of the jacketed sample prior to deformation. Modified after Pec et al. (2012).

(http://www.ImageSXM.org.uk) and the 'Lazy pole' macro from the CIP database (https://earth.unibas.ch/micro/). Lower hemisphere projections are used to plot the quartz c-axes.

2.4. Data processing

The Griggs apparatus uses an external load cell to measure the force applied to the sample column. The displacement of the σ_1 piston is measured using a direct current displacement transducer with a resolution of 1 μm. Experimental data are digitally recorded at a sampling rate of 1 Hz and processed by the open source MATLAB program RIG (http://mpec.scripts.mit.edu/peclab/software/). Piston displacement was corrected for apparatus compliance while the force was corrected for friction based on a set of calibration tests. The samples thin by ~40% in the high strain experiments; we assume that the thinning is continuous with increasing piston displacement. The mechanical data are corrected for shear zone thinning and forcing block area change with increasing shear strain, as well as variations in confining pressure. Shear stresses and shear strain rates were converted to equivalent stress ($\sigma_{eqv} = 2\tau$ were τ is shear stress) and equivalent strain rate ($\dot{\varepsilon}_{eqv} = \frac{\dot{\gamma}}{\sqrt{3}}$, where $\dot{\gamma}$ is shear strain). All experimental data are summarized in Table 1.

Table 1
Experimental conditions.
Synthetic Quartz-Muscovite Aggregates Annealed and Deformed in General Shear at T = 800 °C and P = 1.5 GPa.

Experiment No.	Ms. (%)	Shear strain, γ	Shear strain rate, $\dot{\gamma}$ (s^{-1})	Shear stress[a], τ (MPa)	Final Thickness, (mm)
372LT	0	0	0	0	1.60
394LT	5	0	0	0	1.60
396LT	10	0	0	0	1.70
398LT	25	0	0	0	1.70
370LT	0	0.7	1.3×10^{-5}	535	1.40
385LT	5	0.6	1.3×10^{-5}	283	1.40
390LT	10	0.5	1.2×10^{-5}	178	1.45
392LT	25	0.6	1.5×10^{-5}	81	1.45
379LT	0	3.9	1.6×10^{-5}	310	0.95
382LT	5	3.9	2.7×10^{-5}	224	1.00
389LT	10	4.3	3.2×10^{-5}	170	0.90
391LT	25	4.0	3.2×10^{-5}	60	0.90

[a] The shear stress listed in Table 1 is the final stress.

3. Results

3.1. Mechanical data

As shown in Fig. 2, sample strengths decrease with an increase in muscovite content. This result is consistent with previous experimental studies on polyphase aggregates that analyzed the influence of increasing amounts of weaker phases, including halite–calcite (Jordan, 1987), muscovite–quartz (Tullis and Wenk, 1994), camphor–octachloropropane (Bons and Urai, 1994), and anorthite–diopside (Dimanov and Dresen, 2005). The pure quartz high strain sample reached a peak shear stress of 440 MPa at $\gamma \approx 0.8$, followed by strain weakening to a stress of 285 MPa at $\gamma \approx 2.4$ and a nonlinear increase in stress to 310 MPa at $\gamma \approx 4.0$. In comparison, the 25% muscovite sample
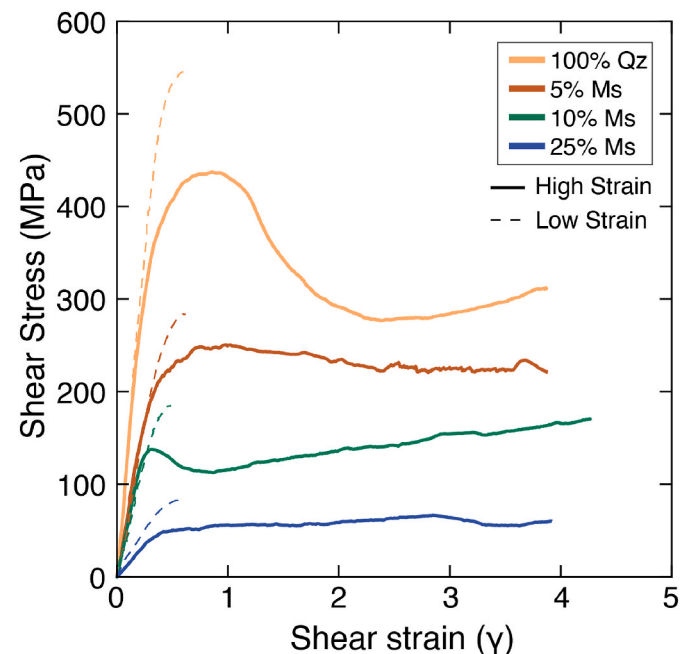

Fig. 2. Plot of shear stress versus shear strain for the peak stress/low strain (dashed lines) and high strain (solid lines) experiments.

only achieved a steady state flow stress of 60 MPa and no strain weakening is observed. The magnitude of strain weakening observed for muscovite-bearing samples with 5% and 10% muscovite is more modest than that observed for the pure quartz sample. The low strain experiments all record higher shear stresses than the high strain experiments for the same volume percent of muscovite; however, the variation in stress for all the muscovite-bearing samples, for the same volume percent of muscovite, are approximately within experimental error (±30 MPa, Holyoke and Kronenberg, 2010). While the low strain pure quartz sample is stronger than the high strain sample, they are both consistent with previous experiments on quartz deformed at similar deformation conditions in the shear geometry (Supplementary Fig. S1). The raw mechanical data and hit point calculations are plotted in Supplementary Fig. S2.

3.2. Microstructural observations

Here we outline the microstructural characteristics of the hydrostatically annealed and deformed samples to illustrate how the presence of muscovite influences the amount of dynamic recrystallization, the development of S–C–C' fabrics and the evolution of quartz CPO.

3.2.1. Hydrostatically annealed samples

Hydrostatically annealed samples help characterize the microstructure prior to deformation. Quartz grains in all hydrostatically annealed samples show undulatory extinction, and evidence for grain crushing and microcracking; the crushed material heals to form small grains ranging from 10 to 15 μm in diameter (Fig. 3). We interpret that grain crushing and microcracking occur during pressurization of the originally porous sample, where grain boundaries and microcracks within crushed quartz can be filled with smaller neocrystallized muscovite (see green arrows in Fig. 3d and Supplementary Fig. S3). Neocrystallized muscovite
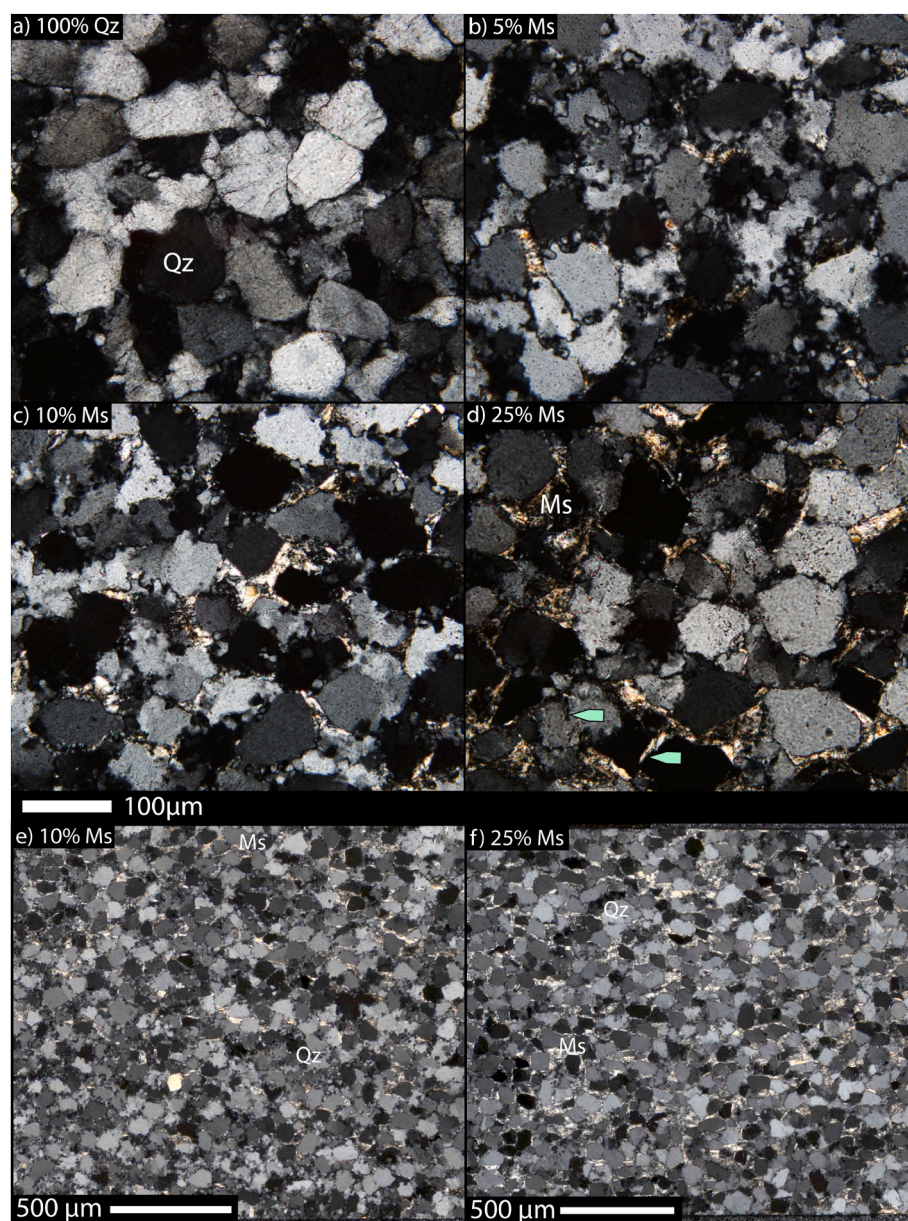
Fig. 3. Polarized light microstructures of quartz-muscovite samples at hydrostatic conditions. The shear plane is parallel to the horizontal plane of each micrograph. Photomicrographs taken in cross-polarized light. Qz – quartz and Ms – muscovite. d) green arrows show muscovite within quartz microcracks. (For interpretation of the references to color in this figure legend, the reader is referred to the Web version of this article.)

grains are defined as new muscovite grains, interpreted to form either through dissolution and precipitation or compositional change. EDS analysis shows the neocrystallized muscovite are in fact muscovite and not a reaction product from any potential muscovite breakdown reaction (Supplementary Fig. S4). In the muscovite-bearing samples, the muscovite grains do not develop a strong preferred orientation; however, a notable amount of muscovite aligns sub-parallel to the shear plane in the 10% and 25% muscovite samples (Fig. 3c–f), while in the 5% muscovite sample, muscovite grains are mostly isolated (Fig. 3b). Grain crushing in quartz is most prominent in the pure quartz, 5% and 10% muscovite samples. All muscovite-bearing samples show minor amounts of reaction products (Supplementary Fig. S3).

3.2.2. Low strain (peak stress) samples

The effect of muscovite on microstructural evolution is minimal at low strains. The low strain samples, which achieve peak stress between $\gamma = 0.5$–0.75, develop weak foliations defined primarily by the SPO of quartz in the pure quartz and 5% muscovite samples and by both the SPO of quartz and muscovite in the 10% and 25% muscovite samples

(Fig. 4). In the pure quartz sample, a foliation defined by the shape of relict quartz grains developed at an angle 35–40° antithetic to the shear plane, where antithetic refers to rotations opposite the shearing direction with the shear plane representing 0°. This sample also shows a higher fraction of recrystallized grains in bands parallel to the foliation plane. In the 5% and 10% muscovite samples, a foliation formed ~30° antithetic to the shear plane; the muscovite grains in the 5% muscovite sample remain isolated with no obvious SPO, while muscovite grains are more interconnected in the 10% muscovite sample (Fig. 4c). At the sample-scale, the 25% muscovite sample has a weak foliation defined primarily by an SPO of muscovite oriented 15° antithetic from the shear plane (Fig. 4f), a much lower angle than observed in the other low strain experiments. Similar to the hydrostatic experiments, the 10% and 25% muscovite samples have a notable number of muscovite grains oriented sub-parallel to the shear plane (Fig. 4e and f). Fine extinction bands, as defined by Derez et al., 2015, are observed in relict quartz grains in all low strain samples (Fig. 4). All muscovite-bearing samples have minor amounts of reaction products (Supplementary Fig. S5).

In comparison to the pure quartz sample, dynamic recrystallization
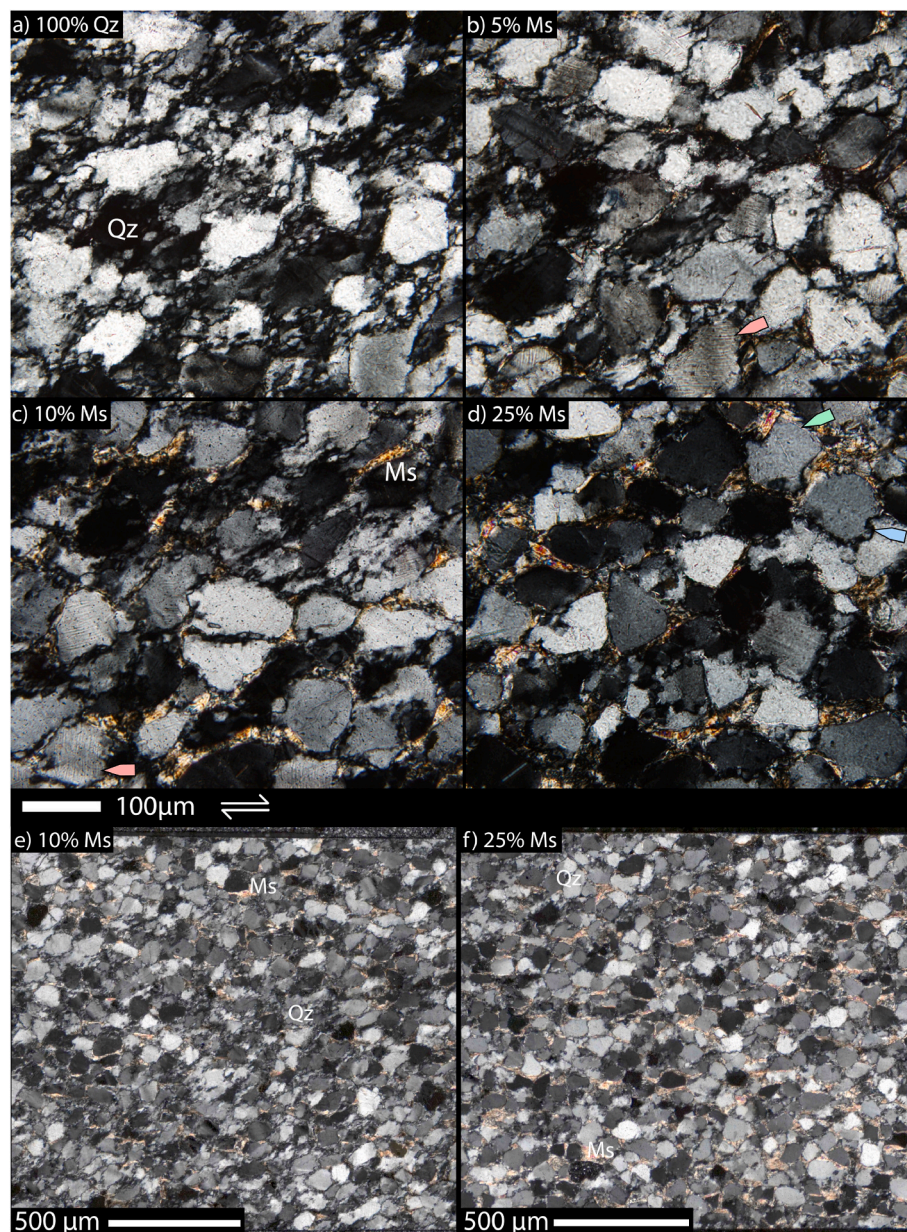
Fig. 4. Polarized light microstructures of quartz-muscovite samples at low strain. Shear plane is parallel with the horizontal plane of each micrograph with a dextral sense of shear. Photomicrographs taken in cross-polarized light. Qz – quartz and Ms – muscovite. Red arrows in b,c) show examples of quartz grains with deformation lamellae. k The green arrow in d) shows an example of a quartz-muscovite phase boundary and the blue arrow shows an example of a quartz-quartz grain boundary. (For interpretation of the references to color in this figure legend, the reader is referred to the Web version of this article.)

of quartz is less extensive in the muscovite-bearing samples (Fig. 4), with the 25% muscovite sample showing the least amount of quartz recrystallization (Fig. 4). In the muscovite-bearing samples, dynamic recrystallization occurs at quartz grain boundaries and is rarely observed at quartz-muscovite phases boundaries (Fig. 4).

3.2.3. High strain samples

At high strains, the quartz microstructures change dramatically with an increase in muscovite content (Figs. 5 and 6). The extent of dynamic recrystallization in quartz decreases as the volume percent of muscovite increases. Microstructures for the pure quartz sample indicate homogenous deformation with near complete (>97%) dynamic recrystallization (Figs. 5a and 6a). Relict quartz grains form elongated ribbons in an orientation consistent with the imposed shear direction, defining a foliation ~12° antithetic from the shear plane (Fig. 5a). Additionally, fine extinction bands are observed in relict quartz grains in all high strain samples (Figs. 5–7 and Supplementary Fig. S6). The 5% muscovite sample shows ~85% dynamic recrystallization of quartz, while the majority of muscovite grains in the 5% muscovite sample align at a small angle (<10°) to the shear plane (i.e., close to the C-plane), and "mica fish" are observed in orientations consistent with the imposed sense of shear (Figs. 5b and 6b). Many muscovite grains remain isolated, with shapes conforming to the adjacent quartz ribbons.

The addition of 10% and 25% muscovite promotes significant changes in the quartz microstructures. The amount of dynamic recrystallization of quartz decreases and the relict quartz grains remain more equant, indicating smaller amounts of intragranular strain. For example, muscovite-filled quartz microcracks, where the cracks are interpreted to form during pressurization similar to Fig. 3d, can be observed in the high strain 25% muscovite sample (Fig. 7a). In the 10% muscovite sample, ~30% dynamic recrystallization is observed (Figs. 5c and 6c). Relict quartz grains in the 10% muscovite sample are moderately elongated and rotate in the direction of shear, producing an SPO and partly defining a foliation oriented 20–25° antithetic from the shear plane

(Fig. 5c). Only ~5% dynamic recrystallization is observed in the 25% muscovite sample, where recrystallization is primarily localized at quartz-quartz grain boundaries (Figs. 5d and 6d). Relict quartz grains are only modestly elongated in the 25% muscovite sample, but still define a foliation oriented ~20° antithetic from the shear plane. All high strain muscovite-bearing samples exhibit minor amounts of reaction products at muscovite grain boundaries that can be observed from the bright needle-shaped grains in Fig. 9a and Supplementary Fig. S7. These reaction products may indicate a change in chemical composition of the muscovite, while the muscovite can still be identified as muscovite.

All muscovite-bearing samples deformed to high strains develop muscovite-rich (Ms) C'- bands. These shear bands are sub-planar (i.e., sub-linear in 2D) and are distributed throughout the sample. In the 5% muscovite sample, Ms C'-bands develop at an orientation ~30° synthetic to the shear plane and extend up to 150 μm in length (Figs. 6b and 8). Ms C'-bands in the 10% muscovite sample develop at a wider range of orientations than in the 5% muscovite sample, ranging from 15 to 30° synthetic to the shear plane, and are typically longer than the Ms C'-bands observed in the 5% muscovite sample, extending up to 500 μm in length (Fig. 6c). In the 25% muscovite sample, muscovite is weakly interconnected throughout the sample producing more numerous, but less distinct Ms C'-bands (Fig. 6d).

Another microstructural feature that develops along C'-planes in all the high strain muscovite-bearing samples are linear bands defined primarily by recrystallized quartz grains and pores (interpreted to have been fluid-filled during the experiment) that often extend from muscovite grains (Fig. 9a). We call these features C'-bands because they are also sub-planar and form in the same orientation as the Ms C'-bands. The majority of C'-bands do not contain muscovite (Fig. 9a), however there are some C'-bands that contain a small amount of neocrystallized muscovite and in a few cases, the C'-bands contain a mixture of quartz and neocrystallized muscovite (Fig. 9b and c). C'-bands range in length up to 100 μm and are typically defined by the spacing between muscovite grains (Fig. 9). In the 5% and 10% muscovite samples, local
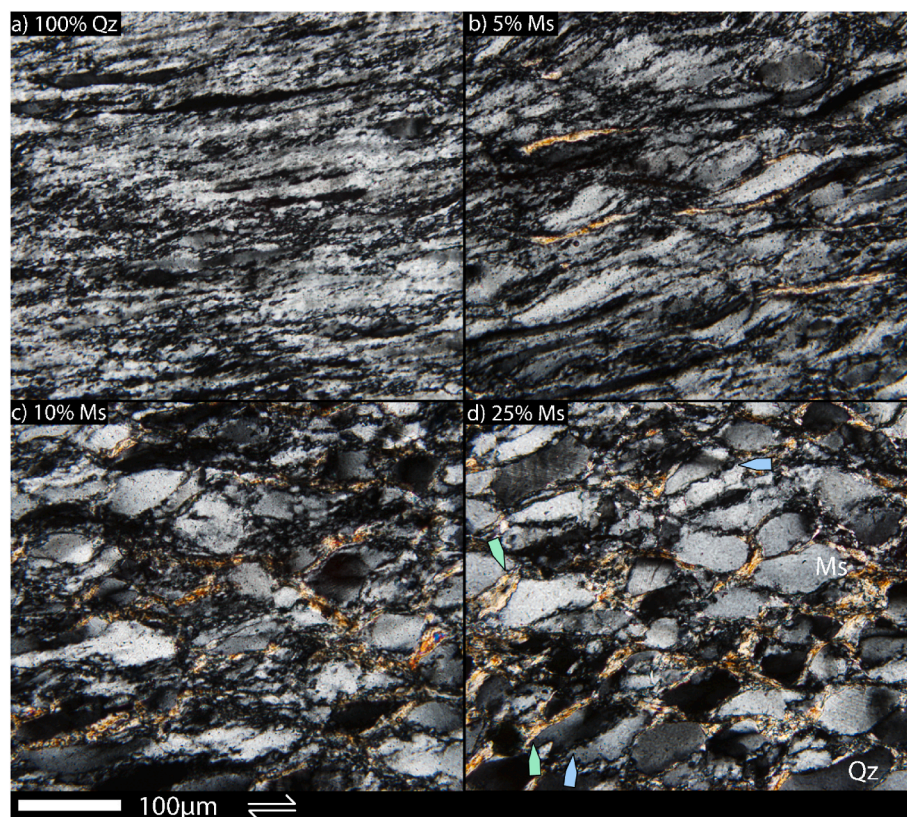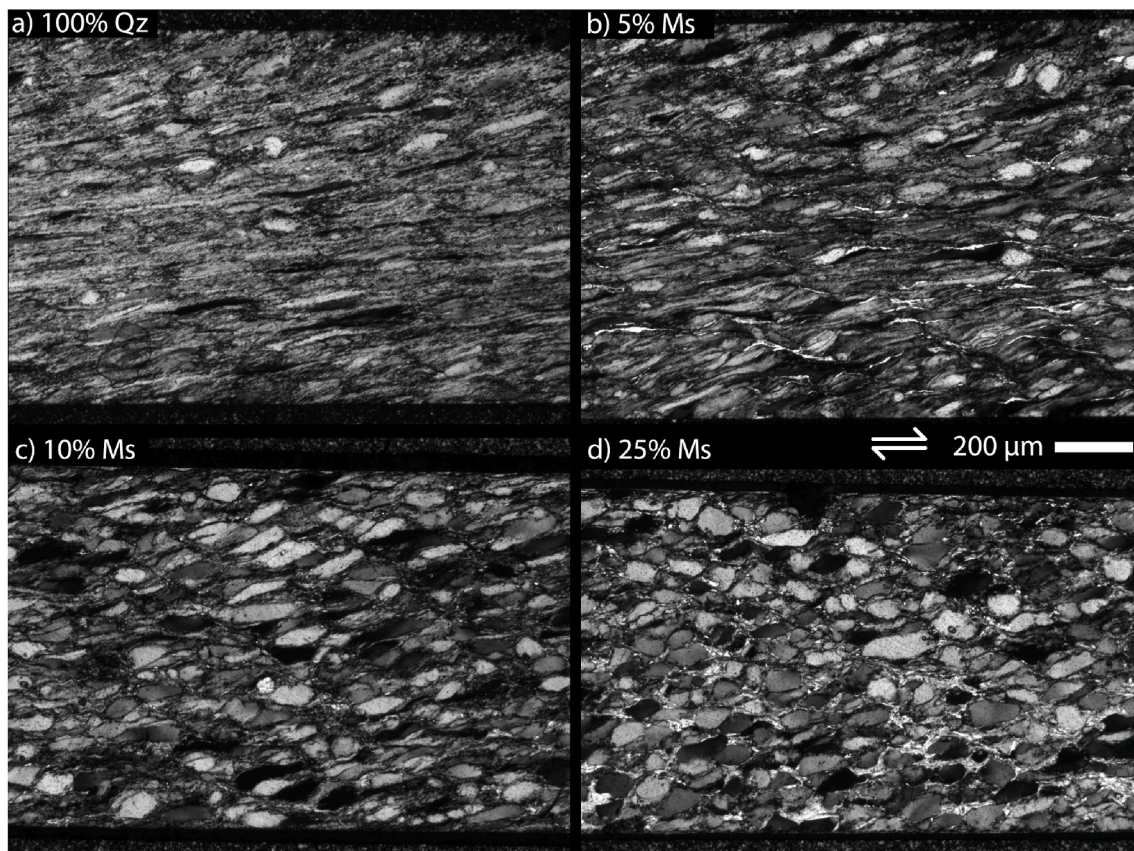

Fig. 5. Polarized light microstructures of quartz-muscovite samples at high strain. d) Blue arrows highlight quartz-quartz grain boundaries while green arrows highlight quartz-muscovite phase boundaries. Shear plane is parallel with the horizontal plane of each micrograph with a dextral sense of shear. Photomicrographs taken in cross-polarized light. Qz – quartz and Ms – muscovite. (For interpretation of the references to color in this figure legend, the reader is referred to the Web version of this article.)

Fig. 6. Polarized light microstructures of the high strain samples using a circular polarizer. Shear plane is parallel with the horizontal plane of each micrograph with a dextral sense of shear. The color of quartz ranges from black to light grey while muscovite is distinctively lighter grey to white. In the 10% muscovite sample, the muscovite grains are a darker grey but still distinguishable due to their characteristic shape and orientation. In each micrograph, the alumina shear piston(s) can be observed in the top and/or bottom of each photo for reference.
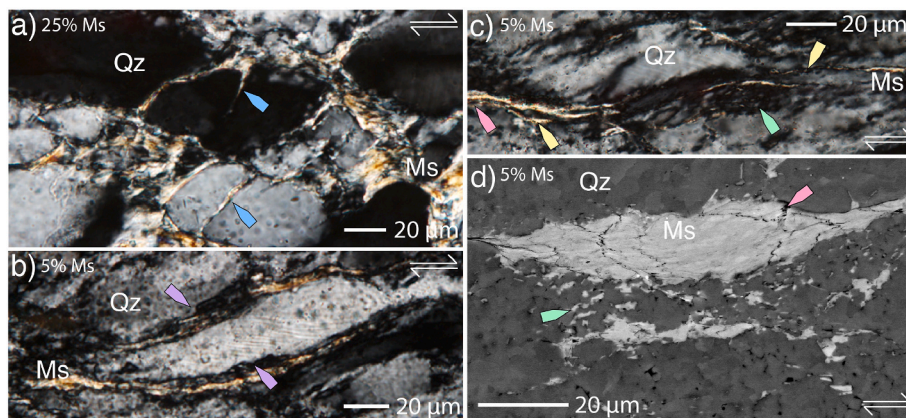
Fig. 7. Cross-polarized light and backscatter electron photomicrographs from the high strain muscovite-bearing samples. a) blue arrows highlight muscovite filling an intragranular crack in two quartz grains. b) purple arrows highlight serrated phase boundaries at quartz-muscovite phase boundaries where the arrows define the high stress orientation. c,d) Examples of phase mixing between dynamically recrystallized quartz and neocrystallized muscovite highlighted by green arrows, where red arrows highlight relict muscovite grains. c) also shows two examples where recrystallized quartz grains are pinned by muscovite (yellow arrows). The shear plane is parallel with the horizontal plane of each micrograph with a dextral sense of shear. (For interpretation of the references to color in this figure legend, the reader is referred to the Web version of this article.)

phase mixing is observed where muscovite grains are intermixed with dynamically recrystallized quartz grains (Fig. 7c and d, 8). Regions of phase mixing occur sub-parallel to the C-plane between two quartz grains or in the C′-plane with modest amounts of dynamic recrystallization. Phase mixing is not as prevalent in the 25% muscovite sample, with mixing primarily localized to the C′-planes, presumably due to a lack of quartz recrystallization.

Quartz grains that are bounded by muscovite appear to deform homogeneously without recrystallizing (e.g., Fig. 5d); microstructures illustrating this "shielding" effect of muscovite are present in all the muscovite-bearing samples (Figs. 4–6). This observation suggests a

relaxation of strain compatibility constraints at muscovite-quartz phase boundaries by easy slip in the muscovite, which reduces strain rate gradients (and thus dynamic recrystallization) within the relict quartz grains.

Microstructural evidence for quartz and muscovite dissolution is observed in all muscovite-bearing high strain samples. Serrated quartz-muscovite phase boundaries in high stress orientations are observed locally in all the high strain muscovite-bearing samples (Fig. 7b). The serrated phase boundaries are normal to σ_1, a favorable orientation for quartz dissolution (e.g., Shimizu, 1995). In addition, Figs. 7–9 show neocrystallized muscovite grains aligned subparallel to the shear plane
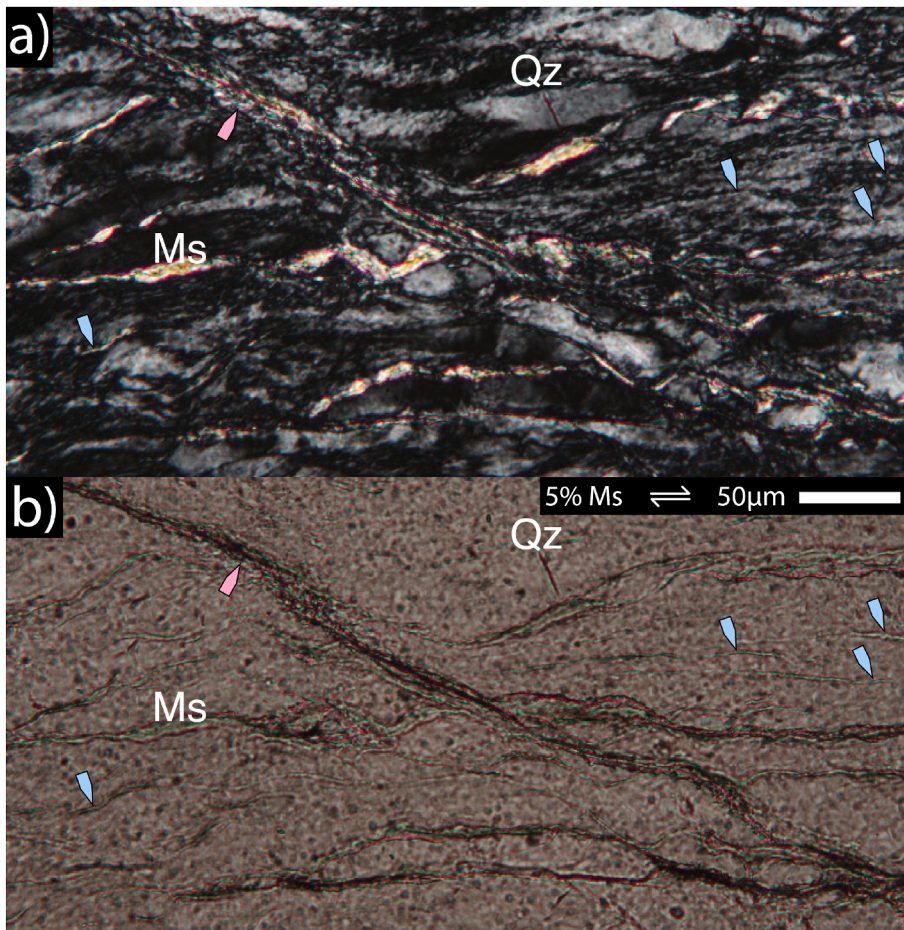
Fig. 8. Cross-polarized and plane light micrographs of high strain 5% muscovite sample. Shear plane is parallel with the horizontal plane with a dextral sense of shear. Ms C′-band defined by alignment of muscovite in the C′-orientation in a) cross-polarized light and b) plane light (highlighted by the red arrows). Blue arrows show several examples of neocrystallized muscovite grains aligned in the C-plane. Qz – quartz and Ms – muscovite. (For interpretation of the references to color in this figure legend, the reader is referred to the Web version of this article.)
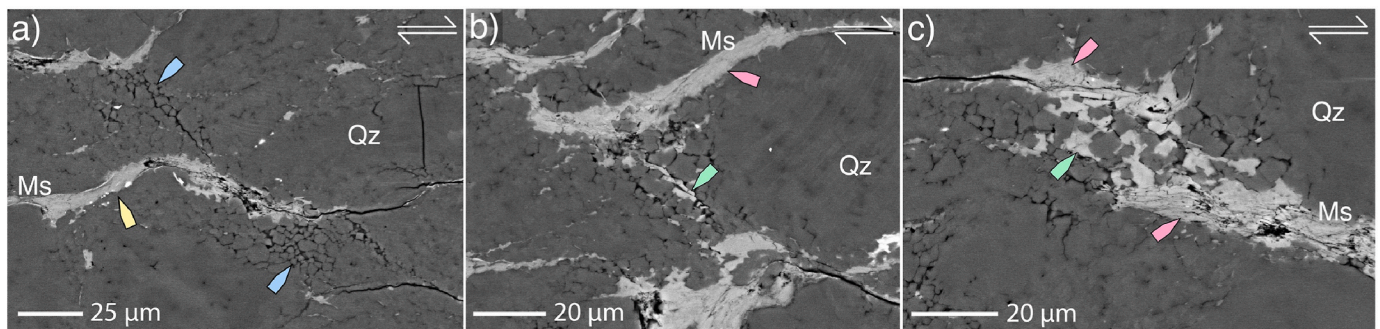
Fig. 9. Backscatter Electron images of C′-bands in the 10% muscovite sample that originate and terminate at the tip of muscovite grains. a) C′- bands are largely made of equant quartz grains and surrounded by void space highlighted by blue arrows. b) An example of neocrystallized muscovite (green arrows) mixing with recrystallized quartz grains and c) shows an example where there is significant mixing between neocrystallized muscovite (green arrow) and recrystallized quartz. b, c) Red arrows highlight relict/original muscovite grains. The yellow arrow in a) highlights potential reaction products from muscovite compositional change. The shear plane is parallel with the horizontal plane of each micrograph with a dextral sense of shear. Muscovite (Ms) grains are lighter grey and quartz (Qz) darker grey. Portions of muscovite grains are plucked during sample preparation. (For interpretation of the references to color in this figure legend, the reader is referred to the Web version of this article.)

in regions of quartz recrystallization, suggesting neocrystallized muscovite grew in these locations at hydrostatic conditions or during deformation. Based on the deformation microstructures, most neocrystallized muscovite grains are observed at distances of ~20–30 μm from relict muscovite grains (Fig. 7c and d, 9) but a few grains are observed at distances up to ~100 μm (see blue arrows in Fig. 8).

3.2.4. Shape Preferred Orientations (SPO)

The SPO of relict quartz grains systematically decreases with an increase in muscovite content (Fig. 10). In hydrostatic samples, the pure quartz, 5%, and 10% muscovite samples all exhibit nearly random SPOs with average grain aspect ratios of 1.08, 1.03, and 1.03, respectively. The 25% muscovite hydrostatic sample shows a weak SPO with a long axis oriented ~25° antithetic with respect to the shear plane with an average grain aspect ratio of 1.15 (Fig. 10).

At low strain, the role of muscovite on SPO is minimal, except for the sample with 25% muscovite. The pure quartz, 5%, and 10% muscovite samples all show an SPO with long axes oriented 25–30° antithetic to the
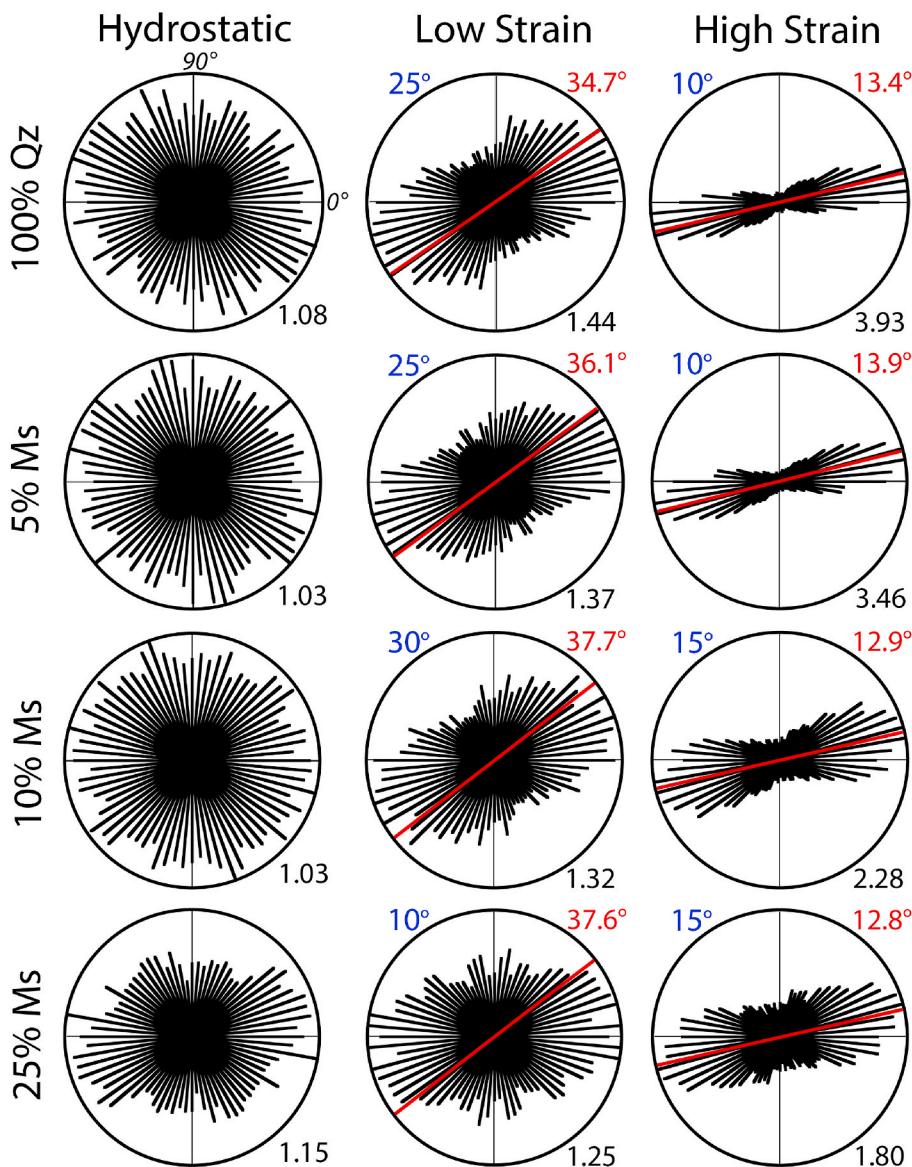
Fig. 10. Surface orientation distribution (SURFOR) functions of relict quartz grains for all quartz–muscovite samples. The aspect ratio for each sample is plotted in black in the bottom right. The red line represents the expected orientation of the long axis of the finite strain ellipse (red numbers indicating the expected angle between the long axis of the strain ellipse with the shear plane). The measured angle between the maximum of the rose diagram and the shear plane is represented in blue in the top left, where 0° is parallel with the shear plane. The shear plane is in the east-west orientation with a dextral sense of shear. (For interpretation of the references to color in this figure legend, the reader is referred to the Web version of this article.)

shear plane and similar grain aspect ratios of 1.44, 1.37, and 1.32, respectively. In contrast, the 25% muscovite sample has a long axis oriented ~15° antithetic to the shear plane with an aspect ratio of 1.25 (Fig. 10); this SPO likely reflects the influence of an initial SPO, as observed in the 25% muscovite hydrostatic sample. The quartz grain aspect ratios for the low strain samples decrease modestly, but systematically with increasing muscovite content.

The influence of muscovite on quartz SPO is more obvious at high strain. The pure quartz and 5% muscovite samples exhibit quartz SPOs with long axes oriented 10–15° antithetic from the shear plane with average aspect ratios of 3.93 and 3.46, respectively. The long axes for the 10% and 25% muscovite samples are oriented 15–20° antithetic from the shear plane with average aspect ratios of 2.28 and 1.80, respectively. In high strain samples, the particle long-axis maxima are oriented approximately parallel to the finite elongation direction calculated based on the sample strain (Fig. 10). For the low strain samples, the particle long-axis maxima are oriented near the finite elongation direction but rotated further towards the shear plane (Fig. 10).

Plotting the quartz porphyroclast aspect ratio against both the normalized frequency and orientation of the long particle axis for all the samples emphasizes the influence of muscovite on the evolution of

quartz SPO (Fig. 11). The change in aspect ratio between the hydrostatic and high strain samples decreases systematically with increasing muscovite content. The pure quartz and 5% muscovite samples show a significant increase in the aspect ratio from the hydrostatic sample to the high strain sample, while there is only a minimal change in the aspect ratio with strain in the 10% and 25% muscovite samples. In the pure quartz and 5% muscovite high strain samples, large aspect ratio grains or "ribbon" grains are observed; while in the 10% and 25% muscovite high strain samples no large aspect ratio grains are observed (Fig. 11). Quartz ribbons are orientated within ~15° of the shear plane. Quartz grains with smaller aspect ratios show a greater spread in the long axis orientations with orientations as high as 35° away from the shear plane in the pure quartz and 5% muscovite samples and 40° in the 10% and 25% muscovite samples (Fig. 11).

3.2.5. Crystallographic Preferred Orientation (CPO)

Muscovite content also influences the development of quartz CPO, where Fig. 12 shows the pole figures and pole figure maximum (multiples of a uniform distribution) for all samples. Fig. 13 shows the CIP maps for the high strain samples. Grain boundary maps of relict quartz grains were constructed from the CIP maps in Fig. 13 of the high strain samples to highlight variations in quartz strain based on c-axis
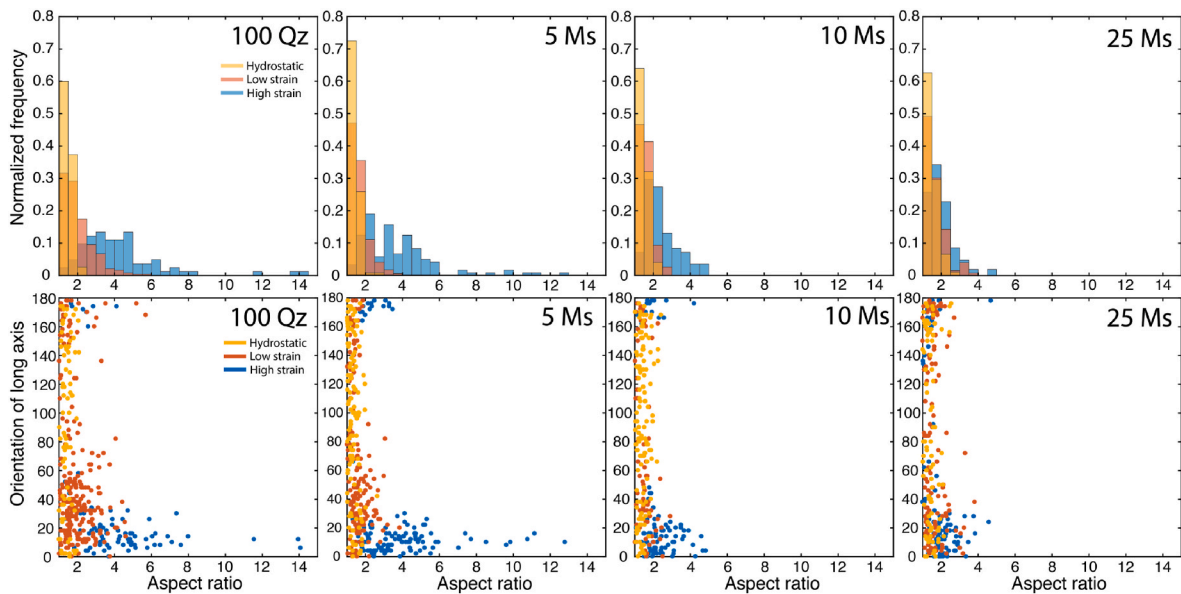
Fig. 11. The top row shows plots of quartz grain aspect ratio versus normalized frequency for the hydrostatic, low strain, and high strain samples. The bottom row shows plots of aspect ratio versus orientation of the long particle axis for the hydrostatic, low strain, and high strain samples. 0 and 180 represent the orientation of the shear plane. The data used to construct these plots comes from the same SURFOR analyses used to plot the rose diagrams in Fig. 10. Long axis angle orientations follow the same convention used in Fig. 10.
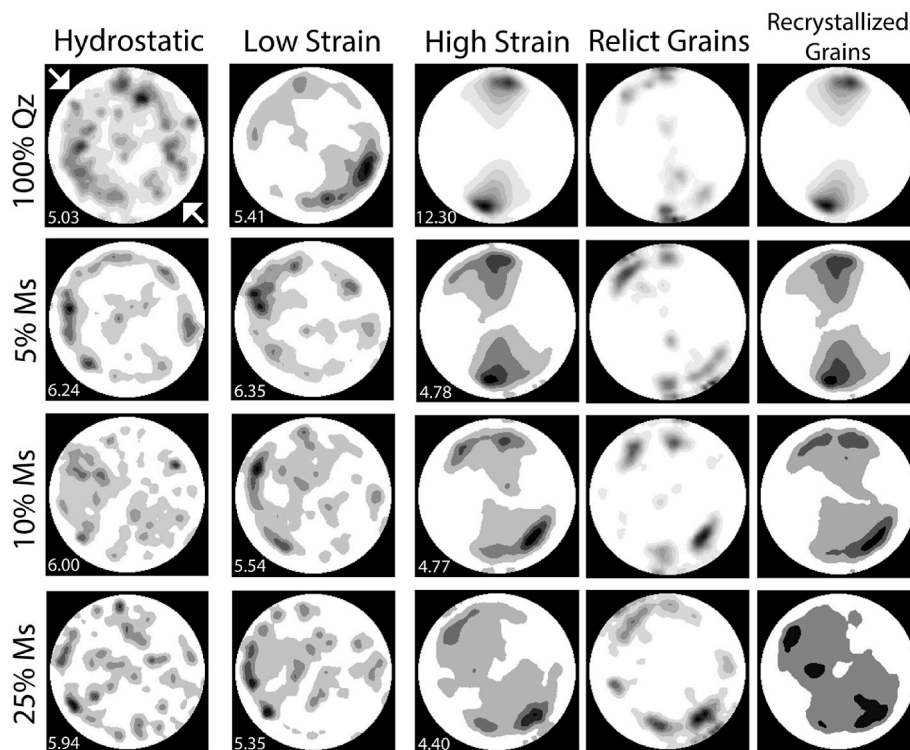
Fig. 12. Area-weighted pole figures for quartz c-axis orientations. Contours are set at 0.5 times the uniform distribution with maxima for each pole figure presented to the bottom left of each corresponding pole figure. The shear plane is in the east-west orientation with a dextral sense of shear. The white arrows around the 100% quartz hydrostatic pole figure define the axial shortening direction.

orientations (Fig. 14).

All the hydrostatic samples exhibit a random quartz c-axis texture (Fig. 12). The CIP maps for the hydrostatic and low strain samples are illustrated in Supplementary Figs. S8 and S9, respectively. Crushed quartz grains in the hydrostatic samples are easily identified in the CIP maps, displaying a significantly smaller grain size, 10–15 μm, than the starting grain size (Supplementary Fig. S10).

At low strains, the pure quartz sample develops a quartz CPO with c-axes aligned sub-parallel to the axial shortening direction (Fig. 12).

In high strain samples, the strength of the quartz CPO decreases with increasing muscovite content. In addition, the orientation of the CPO with respect to the shear plane varies with muscovite content (Fig. 12). In the 100% quartz sample, c-axes align approximately normal to the shear plane, rotated slightly synthetically with the sense of shear,
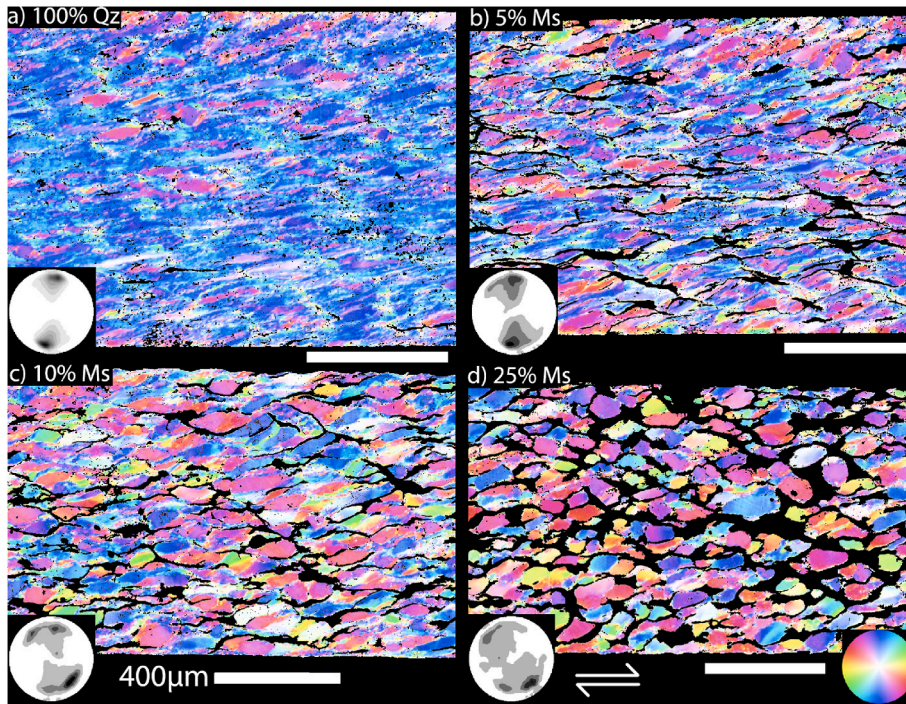
Fig. 13. C-axis orientation images of quartz for the high strain samples. Corresponding pole figures for each orientation map are located in the bottom left corner. The shear plane for each map is parallel to the horizontal plane of the image with a dextral sense of shear. Color lookup table found in the bottom right of the figure. The scale bar is 400 μm and found at the bottom right for each CIP map. (For interpretation of the references to color in this figure legend, the reader is referred to the Web version of this article.)
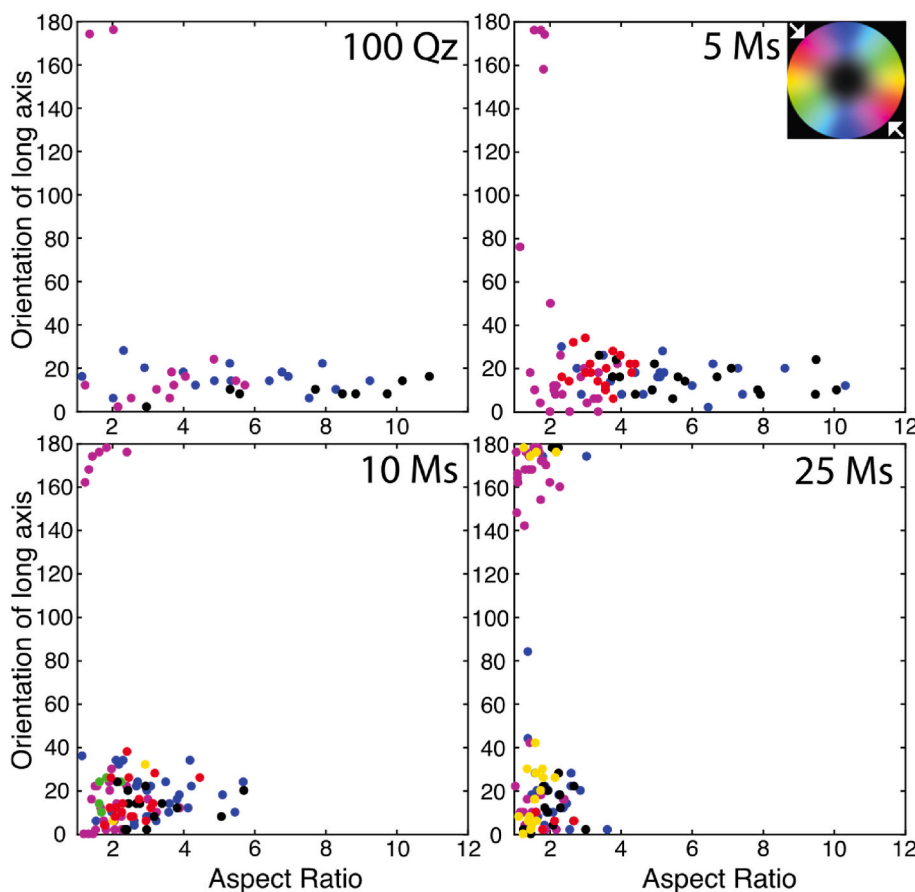

Fig. 14. Plots of aspect ratio versus orientation of the long particle axis for the high strain samples. Data are color-coded to represent the particle (e.g., grains) c-axis orientation. The color lookup table is represented in the top right of figure. 0 and 180 represent the orientation of the shear plane. SURFOR analyses were performed on relict quartz grains from the CIP maps in Fig. 13. The white arrows around the color look up table define the axial shortening direction. Long axis angle orientations follow the same convention used in Fig. 10. (For interpretation of the references to color in this figure legend, the reader is referred to the Web version of this article.)

indicative of dominantly basal <a> slip. With low muscovite contents, c-axes also align normal to the shear plane, but with increasing muscovite content, the c-axis maxima progressively become more parallel to the axial shortening direction.

In Fig. 12 we also highlight differences between the CPO of relict and recrystallized grains as a function of muscovite content. The c-axes of

relict grains in the pure quartz sample are primarily orientated perpendicular to the shear plane (Figs. 12 and 13). In contrast, a larger fraction of c-axes are oriented sub-parallel to the axial shortening direction in all of the muscovite-bearing samples (Figs. 12 and 13). The c-axes for the recrystallized quartz grains show the same spread in orientations as the relict grains but with stronger maxima.

In Fig. 14 we illustrate relationships between grain aspect ratio, the orientation of the particle long axis, and the c-axis orientations of relict quartz grains from the high strain samples. In all samples, quartz grains with Y-max c-axis orientations (c-axes align parallel to the Y direction of the strain ellipse) or with c-planes parallel to the shear plane have the largest aspect ratios, suggesting that the dominant slip systems are basal <a> and prism <a> slip, consistent with single crystal data (Muto et al., 2011; Stünitz et al., 2017). In the 10% and 25% muscovite samples, the number of grains with c-axes oriented antithetically to the shear plane increases. These have similar low aspect ratios to grains oriented with c-axes sub-parallel to the shear plane. The lower degree CPO and more variable rotation of quartz grains suggests that as the volume percent of muscovite increases, more strain is partitioned into muscovite and less strain is accommodated by quartz.

4. Discussion

Our results demonstrate that muscovite plays an important role on the strength and microstructural evolution of mica-bearing quartzites. Below we discuss how the observed changes in microstructural development constrain the role of muscovite on grain scale deformation processes and compare our results to a combination of flow laws and rheological models for the aggregate viscosity of a mica-bearing quartzite.

4.1. Effect of muscovite on the development of c-axis fabrics in quartz

Muscovite plays an important role in the development of quartz c-axis fabrics in our deformed samples. At low strains, where only modest dynamic recrystallization is achieved, some c-axes in the pure quartz sample align sub-parallel to the axial shortening direction, consistent with previous general shear quartz experiments (Heilbronner and Tullis, 2006), numerical simulations employing Taylor-Bishop-Hill models (Lister et al., 1978; Lister and Hobbs, 1980), and viscoplastic self-consistent (*VPSC*) models (Morales et al., 2011) for quartz in shear. At high strains, with a high degree of dynamic recrystallization, the c-axes align approximately normal to the shear plane, indicative of dominantly basal <a> slip (Figs. 12 and 13), which is also consistent with previous experimental work on quartz conducted in the general shear geometry at similar deformation conditions (Heilbronner and Tullis, 2006; Richter et al., 2018). These observations suggest that as the sample dynamically recrystallizes, the orientation of recrystallized grains and some relict grains rotate synthetically with the shear sense developing preferred orientations of basal planes near the shear plane. However, a significant fraction of relict quartz grains maintains c-axis orientations at large angles to the shear plane, even at shear strains exceeding 4 (see Figs. 7 and 8 in Heilbronner and Tullis, 2006; Richter et al., 2018, and Fig. 13a). For the deformation conditions of our samples, muscovite is mechanically weaker than quartz, and therefore strain is partitioned into muscovite in the muscovite-bearing samples. This results in a lower extent of dynamic recrystallization of quartz in samples with higher muscovite contents and less strain accumulation in quartz. As a result, quartz c-axis rotation into the basal <a> c-axis fabric orientation is suppressed, leaving a larger number of relict quartz grains with c-axes at a large angle to the shear plane.

The development of quartz c-axis fabrics sub-parallel to the axial shortening direction in the high strain muscovite bearing samples may be related to strain partitioning in the quartz-muscovite aggregates, in addition to details of the deformation mechanism of the unrecrystallized relict grains. At low strains, the muscovite-bearing samples show

random quartz c-axis fabrics, while at high strains some quartz c-axes align antithetically to the shear sense, similar to the low strain pure quartz sample, especially the 25% muscovite sample, shows the least amount of dynamic recrystallization in quartz (Fig. 12). In addition, the long axis orientations for the high strain 25% muscovite sample are similar to the low strain pure quartz sample, even though the bulk shear strain in the 25% muscovite high strain sample is ~4 (Fig. 11). These observationst suggest that due to strain partitioning into the weaker muscovite, not enough strain was accumulated in the quartz to produce a c-axis fabric at low strains. Additionally, the similar quartz c-axis fabrics between the low strain pure quartz sample and the high strain muscovite-bearing samples indicate similar processes that lead to the development of the c-axis fabrics sub-parallel to the axial shortening direction. One possibility is the effect of the coaxial shortening in general shear experiments. General shear experiments conducted in the Griggs apparatus contain significant coaxial shortening, where high strain experiments ($\gamma > 3.5$) thin between ~30 and 50% relative to a hydrostatic experiment (Table 1; see also, Heilbronner and Tullis, 2006). If quartz, the more competent and mechanically isotropic phase in the muscovite-bearing samples, accommodates a larger part of the shortening component of the strain and muscovite, the weaker and mechanically anisotropic phase, accommodates the larger part of the simple shear component of the strain, this would lead quartz c-axes to align in the orientation of coaxial shortening. Tullis et al. (1973) have shown that in the absence of dynamic recrystallization quartz grains tend to rotate towards the axial shortening direction, i.e. in our case an antithetic orientation to the shear sense.

Strain partitioning into the muscovite and the suppression of dynamic recrystallization in quartz, may also cause relict quartz grains to deform primarily by glide-dominated dislocation creep without the involvement of grain boundary processes resulting in an antithetically rotated c-axis fabric similar to that in observed in low strain pure quartz experiments (Heilbronner and Tullis 2006), as well as the Taylor-Bishop-Hill and VPSC numerical models (Lister et al., 1978; Lister and Hobbs, 1980; Morales et al., 2011). Through the analysis of a natural shear zone, Kilian et al. (2011b) showed that quartz porphyroclasts (e.g., largely unrecrystallized grains) may align antithetically to the global shear sense if such grains are mechanically stronger than the matrix. The change in c-axis orientation is induced by local kinematics of the unrecrystallized grains during strain partitioning. Such a situation can also arise in our experiments where the unrecrystallized quartz grains represent the mechanically strongest phase of the aggregate. In both models, relict quartz grains will dynamically recrystallize with increasing strain, which can be observed in the 5 and 10% high strain muscovite-bearing samples, however the strain accumulated in the relict quartz grains in the high strain 25% muscovite sample was not high enough to produce significant recrystallization.

The correlation between increasing muscovite content and weakened quartz c-axis fabric in the high strain muscovite-bearing samples is also consistent with the quartz-muscovite axial compression experiments conducted by Tullis and Wenk (1994) as well as naturally deformed micaceous quartzites (Song and Ree, 2007; Little et al., 2015; Hunter et al., 2016, 2019) and graphite bearing quartzites (Krabbendam et al., 2003). The naturally deformed samples analyzed by Song and Ree (2007) and Krabbendam et al. (2003) show a weakening in CPO strength as well as a change to a more random quartz c-axis fabric while the samples analyzed by Little et al. (2015) and Hunter et al. (2016) show a weakening in CPO strength but the general c-axis pattern remains, even though the samples in all four studies cover a wide range in secondary phase abundance.

4.2. Aggregate viscosity

To quantify the influence of muscovite content on the strength of quartz aggregates we compare our results with rheological mixing models. The theoretical bounds to all rheological mixing models for two

phase aggregates are the iso-strain-rate and iso-stress models. In the iso-strain-rate model, which defines the upper strength bound for a two-phase aggregate, the strong and weak phases deform at the same strain rate (i.e., the strong phase must deform at the applied strain rate). The iso-stress model provides a lower strength bound; in this case, both phases deform at the same stress, thereby partitioning more of the strain (strain rate) into the weaker phase. These bounds are defined by equations (1) and (2) for a two-phase quartz-muscovite aggregate,

$$\dot{\varepsilon} = \varphi_{Qz} A'_{Qz} \sigma^{n_{Qz}} e^{\frac{-Q_{Qz}}{RT}} + \varphi_{Ms} A_{Ms} \sigma^{n_{Ms}} e^{\frac{-Q_{Ms}}{RT}} \quad (1)$$

$$\sigma = \varphi_{Qz} \left(\frac{e^{\frac{Q_{Qz}}{RT}}}{A'_{Qz}} \dot{\varepsilon} \right)^{\frac{1}{n_{Qz}}} + \varphi_{Ms} \left(\frac{e^{\frac{Q_{Ms}}{RT}}}{A_{Ms}} \dot{\varepsilon} \right)^{\frac{1}{n_{Ms}}} \quad (2)$$

where φ_i is the volume fraction of quartz (Qz) or muscovite (Ms) and A, Q, and n are the pre-exponential factors, activation enthalpies, and stress exponents of the end-member flow laws (Tullis et al., 1991; Handy 1994). These relationships can be modified to account for a H$_2$O fugacity

term (required for extrapolation to natural conditions); in equations (1) and (2) we denote A' as the preexponential factor times the H$_2$O fugacity term (e.g. $A'_{Qz} = A_{Qz} f'_{H_2O}$) where r is the H$_2$O fugacity exponent.

Tullis et al. (1991) developed an empirical rheological mixing model based on averaging A, Q, and n between the two end-member phases, where the subscript 'agg' refers to the aggregate. The Tullis mixing model is defined by equations (3)–(6); this model does a good job describing the variation in strength of two-phase aggregates with changing phase proportions in axial compression experiments (e.g., anorthite-diopside aggregates; Dimanov and Dresen, 2005).

$$n_{agg} = 10^{\varphi_{Qz} \log (n_{Qz}) + \varphi_{Ms} \log (n_{Ms})} \quad (3)$$

$$A_{agg} = 10^{\left[\frac{\log A_{Qz}(n_{agg} - n_{Ms}) - \log A_{Ms}(n_{agg} - n_{Qz})}{n_{Qz} - n_{Ms}} \right]} \quad (4)$$

$$Q_{agg} = \frac{Q_{Qz}(n_{agg} - n_{Ms}) - Q_{Ms}(n_{agg} - n_{Qz})}{n_{Qz} - n_{Ms}} \quad (5)$$
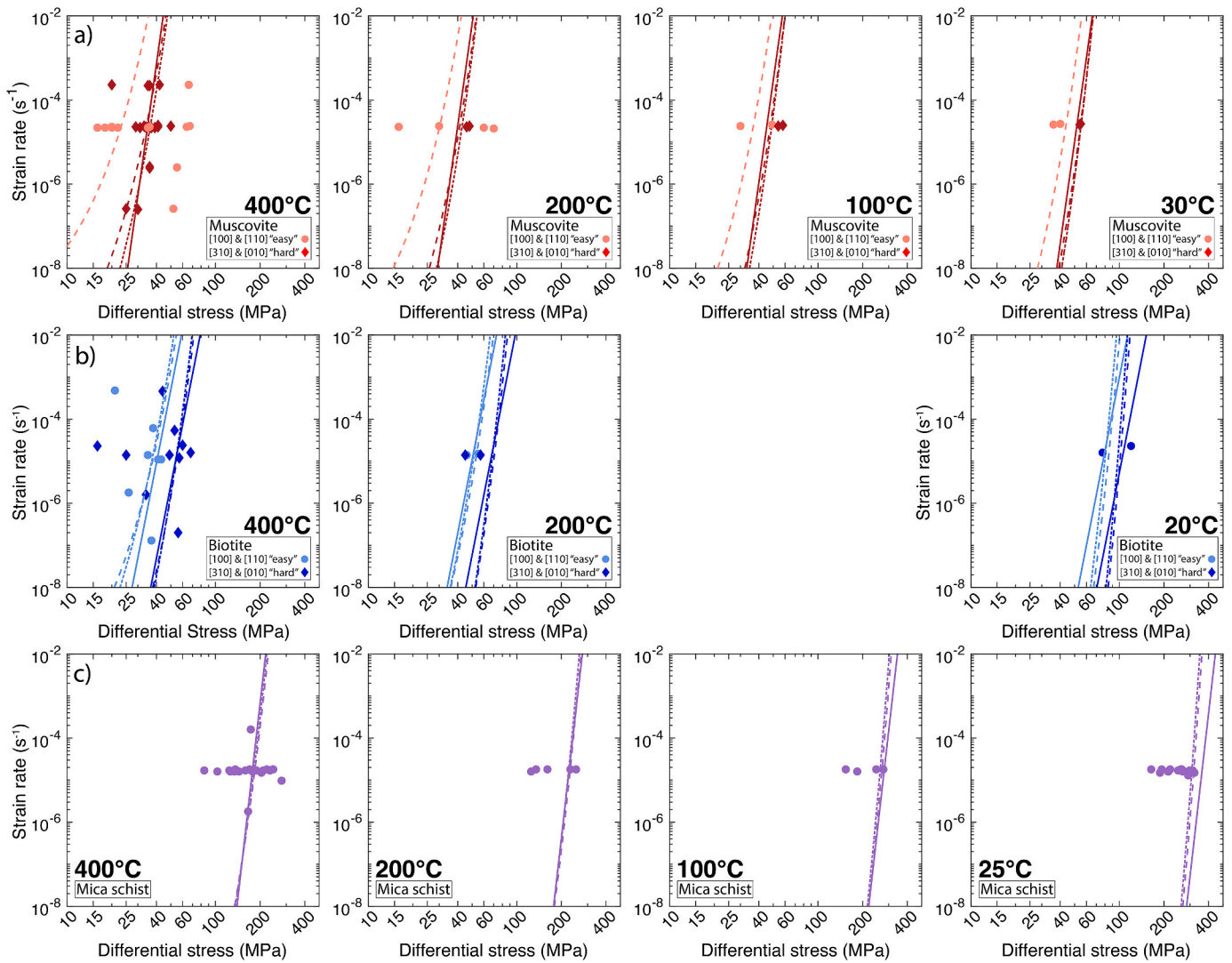
Fig. 15. Plots of differential stress versus strain rate comparing the experimental data for basal slip in a) muscovite from Mares and Kronenberg (1993), b) biotite from Kronenberg et al. (1990), and c) a natural mica schist in the x45z orientation from Shea and Kronenberg (1992). Solid lines represent the respective power law flow laws, the dashed lines represent the exponential flow laws, and the dotted lines represent the exponential flow law that incorporates a stress squared term (see text). Flow law parameters for the biotite and mica schist flow laws incorporating the stress squared term are *Cbio_easy* = 4e-9, *Cbio_hard* = 2e-12, *α_bio* = 0.41, and *Q_bio* = 82 kJ/mol and *C_MS* = 6e-15, *α_MS* = 0.15, and *Q_MS* = 89 kJ/mol, respecitvely. The differential stress plotted for muscovite in Mares and Kronenberg (1993) is the final stress. The confining pressure is not the same for the mechanical data in each plot, however there is no clear pressure dependence within the data and therefore the confining pressure is not distinguished.

$$\dot{\varepsilon} = A_{agg}\sigma^{n_{agg}}e^{\frac{-Q_{agg}}{RT}} \qquad (6)$$

To apply these rheological mixing models, we need power-law flow law parameters for each end-member phase. For this analysis we developed power-law flow law parameters for muscovite based on the mechanical data from Mares and Kronenberg (1993) and used flow law parameters for quartz from Tokle et al. (2019). A limitation to all rheological mixing models is that they are based on the deformation mechanisms modeled by the end member flow laws and do not explicitly account for the possibility of intergranular processes such as grain boundary sliding and pressure solution that may be promoted in multiphase aggregates. In the case of quartz and muscovite, the muscovite flow law was developed based on single crystal deformation experiments where the single crystal was oriented for easy basal slip while the quartz flow law is based on deformation experiments of polycrystalline quartz aggregates. Microstructural evidence from our muscovite-bearing samples suggests grain boundary diffusion processes such as dissolution-precipitation creep are active to some degree (as discussed in the next section); however, there are currently no flow laws available to accurately describe the participation of other mechanisms.

Mares and Kronenberg (1993) define a directional anisotropy for basal slip in muscovite for "easy" slip directions [100] & [110] and "hard" slip directions [310] & [010], similar to biotite (Kronenberg et al., 1990). However, based on the mechanical data from Mares and Kronenberg (1993) it is unclear whether there is directional anisotropy in muscovite (Fig. 15). The mechanical data for samples oriented 45° to the basal plane (001) with slip directions of [310] and [010] provide a good approximation of the average stress for all of the muscovite mechanical data from Mares and Kronenberg (1993) (Fig. 15, Supplementary Fig. S11). Therefore, we use the dataset from experiments with [310] and [010] slip directions to define a power-law flow law for muscovite, with parameters of $n = 25$, $Q = 45$ kJ/mol, and $A = $ 2e-40 MPa^{-n} s^{-1} (see supplementary material). In addition, we use the same mechanical data to develop a new exponential flow law for muscovite incorporating a stress squared term (e.g., dislocation density term) (Frost and Ashby, 1982). The flow law takes the form, $\dot{\varepsilon} = C\sigma^2 \exp\left(\alpha\sigma - \frac{Q}{RT}\right)$, where $C = $ 1e-12, $\alpha = 0.5$, and $Q = 47$ kJ/mol. This process was repeated for biotite and mica schist based on the mechanical data from Kronenberg et al. (1990) and Shea and Kronenberg. (1992), respectively (Fig. 15). These modified exponential flow laws provide a better estimate for mica strength at low stress conditions (Fig. 16 and Supplementary Fig. S14). For reference, we compare the mechanical data and flow laws for muscovite, biotite, and mica schist from Mares and Kronenberg (1993), Kronenberg et al. (1990), and Shea and Kronenberg (1992), respectively, to each other (Fig. 15).

The application of a power-law flow law for muscovite (and biotite) comes with several caveats. Based on both experimental and natural observations, micas appear to deform by glide-controlled mechanisms, referred to as low-temperature plasticity or Peierls creep (Bell et al., 1986; Meike 1989; Kronenberg et al., 1990; Mares and Kronenberg, 1993; Mariani et al., 2006; Aslin et al., 2019), which include exponential relationships with stress and temperature. Application of a power law flow law for micas is thus a simplifying assumption that allows one to estimate the influence of micas on aggregate rheologies through rheological mixing models outlined in equations (3)–(6); however, power law flow laws for micas should not be extrapolated to low stress conditions because of the differences in power law and exponential rheologies (Fig. 16). The creation of voids in kink bands and ripplocations in naturally deformed micas suggests a large activation volume in mica deformation mechanisms, implying pressure could play an important role on the strength of mica. Additionally, if micas are deforming by a glide-controlled mechanism, the stress exponent will be temperature-dependent (Frost and Ashby, 1982; Burdette and Hirth, 2022). Extrapolating mica flow laws to lower stress eclogite facies conditions is also problematic, because the combination of high pressure
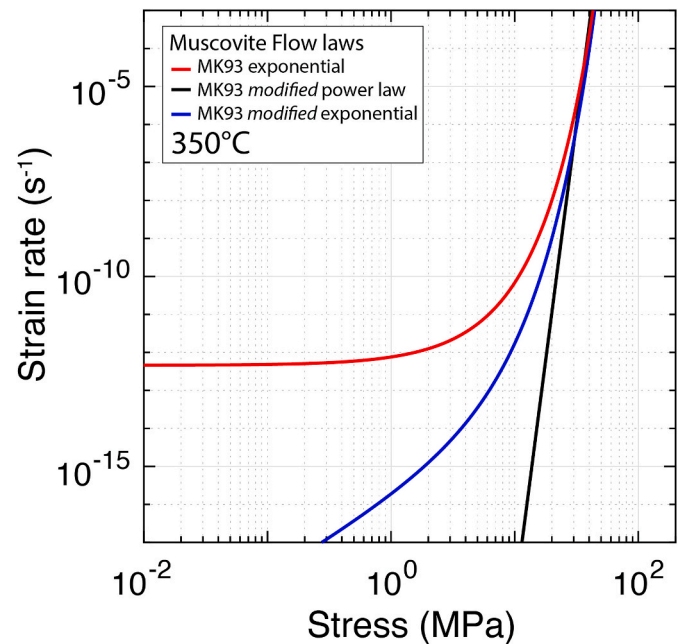

Fig. 16. Plot showing the extrapolation of the exponential muscovite flow law developed by Mares and Kronenberg (1993) [MK93] using the formula: $\dot{\varepsilon} = A\exp(\alpha\sigma)\exp\left(\frac{-Q}{RT}\right)$, and the exponential and power law flow laws developed in this study using the mechanical data from Mares and Kronenberg (1993) labeled *modified*. See the text and supplementary material for flow law equations and mechanical used to derive the flow laws.

and temperature may promote dissolution-precipitation creep, owing to the increased solubility of SiO_2 (e.g., Manning, 2018). However, given these caveats we are confident that the muscovite (and biotite) power law flow laws can be applied to the relatively higher stress geologic conditions from the middle continental crust to near the brittle-plastic transition.

For dislocation creep in quartz, we use flow law parameters of $A = $ 8.3e-13 MPa^{-n} s^{-1}, $n = 3$, $Q = 115$ kJ/mol, and $r = 1.2$ from Tokle and Hirth (2021) (where A is modified from Tokle et al., 2019). The Hirth et al. (2001) flow law significantly underestimates the strength of the high strain pure quartz sample (Fig. 17). Based on this observation, Tokle et al. (2019) compared the mechanical data from 21 experimental studies on dislocation creep in quartz – finding evidence for a transition in the rate-limiting slip system for quartz aggregates with decreasing temperature. The condition where the change in flow law parameters is observed also correlates well with conditions where a transition from prism <a> to basal <a> quartz c-axis fabrics is observed. Our mechanical and CPO data for the pure quartz sample agrees well with the lower temperature flow law constrained by Tokle et al. (2019) (Fig. 17).

To compare the experimental data to the mixing models we use a strain rate of 2×10^{-5} s^{-1} and a water fugacity of 4840 MPa (calculated assuming water-saturated conditions using the data from Pitzer and Sterner (1994) and the Wither's fugacity calculator (https://publish.uwo.ca/~awither5/fugacity/index.htm)). To calculate the effective viscosity, shear stresses and shear strain rates were converted to equivalent stresses ($\sigma_{eqv} = 2\tau$, where τ is shear stress) and equivalent strain rates ($\dot{\varepsilon}_{eqv} = \frac{\dot{\gamma}}{\sqrt{3}}$, where $\dot{\gamma}$ is shear strain rate) (Paterson and Olgaard, 2000), where effective viscosity $= \frac{\sigma_{eqv}}{2\dot{\varepsilon}_{eqv}}$.

At the experimental conditions of this study, the 10% and 25% muscovite samples have an effective viscosity of approximately a factor 2 and 6 lower than the quartz flow law viscosity (Fig. 18a). The rheological mixing model from Tullis et al. (1991) provides an excellent description of the role of muscovite content on the effective viscosity for muscovite contents up to 25% (Fig. 18c).
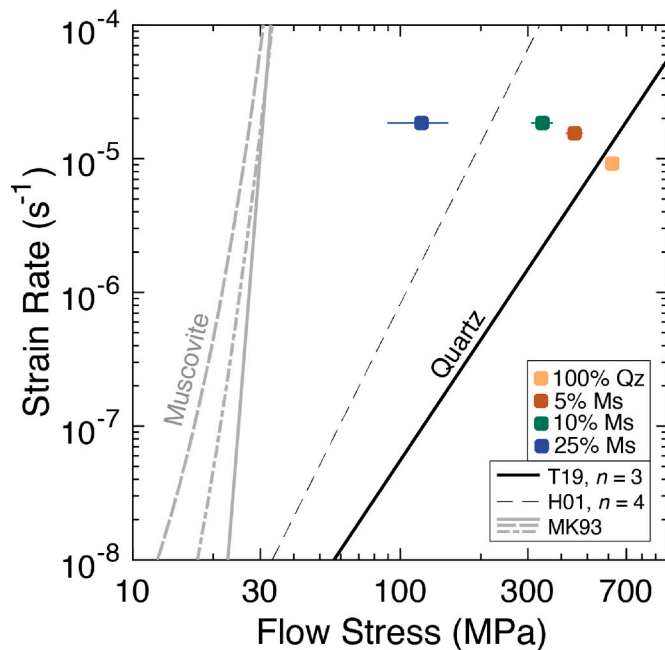
Fig. 17. Plot of log strain rate versus log stress comparing the high strain mechanical data with quartz and muscovite flow laws. The three grey curves are muscovite flow laws developed based on the mechanical data from Mares and Kronenberg (1993) - MK93. The dashed curve (the weakest flow law) is the exponential relationship developed by Mares and Kronenberg (1993). The dash-dot curve is an exponential flow law developed in this study incorporating a stress squared term and the solid line is a power law flow law developed in this study (for flow law parameters, see text). The solid black curve represents the quartz flow law defined by Tokle et al. (2019) - T19 - where A = 8.3e-13 MPa^{-n} s^{-1} and the black dashed curve represents the quartz flow law defined by Hirth et al. (2001) - H01. We use a water fugacity of 4840 MPa for the quartz flow laws. The shear stresses and shear strain rates for the four high strain samples were converted to equivalent stresses and strain rates. Error bars of $\pm$30 MPa are plotted following Holyoke and Kronenberg (2010).

For comparison, previous work on samples deformed in axial compression shows much less weakening with increasing muscovite content (Fig. 18b). As illustrated in Fig. 18d, quartz-muscovite samples deformed in axial compression (Tullis and Wenk, 1994) plot near the iso-strain-rate model. However, the effective viscosity of their pure muscovite sample is significantly greater than that predicted by the single crystal muscovite flow law (Fig. 18d); this observation likely reflects the role of muscovite grain orientation. The muscovite flow law is calibrated using experiments on well-oriented muscovite single-crystals; in the axial compression experiments, the basal planes of the muscovite grains rotate to become sub-perpendicular to the shortening direction, resulting in strain hardening. In contrast, for the general shear geometry, micas often align sub-parallel to the shear plane, which favors easy slip along the basal plane, making the aggregate mechanically weak.

4.3. Deformation mechanisms

Microstructural observations show several deformation mechanisms are active during the deformation experiments. Quartz deforms primarily by dislocation creep where the pure quartz high strain sample develops a strong basal <a> c-axis fabric while in all the deformation experiments quartz shows dynamic recrystallization indicative of dislocation creep (Figs. 4–9). Serrated phase boundaries in contact with muscovite grains sub-orthogonal to the axial shortening direction in both the low and high strain experiments suggest some quartz is dissolved; however, based on microstructural observations the amount of dissolved quartz is limited and localized.

The analysis of the muscovite-bearing samples shows several

deformation mechanisms are active in muscovite. In the high strain muscovite-bearing samples, muscovite grains align parallel to sub-parallel to the shear plane suggesting grain rotation by basal slip. In addition, all muscovite-bearing samples show varying degrees of evidence for neocrystallized muscovite, suggesting a component of dissolution-precipitation creep (Figs. 7–9). Dissolution-precipitation creep is a serial process involving the dissolution, diffusion, and precipitation of material from regions of high stress (i.e., high chemical potential) to low stress and has been well documented in naturally deformed rocks containing micas (Bell and Cuff, 1989; Hippertt, 1994; Wintsch et al., 1995; Wintsch and Yi, 2002; Mulch et al., 2006) and has been proposed to help accommodate shape changes during the formation of mica fish (Mulch et al., 2006). Dissolution-precipitation creep may also be an important deformation mechanism at high strains, where it has been shown that mass transfer by dissolution-precipitation is faster in the direction parallel to the mylonitic foliation than when the micas are at high angles to the foliation (Thompson and Connolly, 1990; Fischer and Paterson, 1992; Zhang et al., 1994; Farver and Yund, 1999). The alignment of muscovite parallel to the shear plane is strain-dependent and all the low and high strain muscovite-bearing samples are weaker than the pure quartz samples (Fig. 2). These observations suggest that either i) there are enough muscovite grains aligned in weak orientations prior to deformation to reduce the strength of the aggregate at low strains through basal slip, ii) another deformation mechanism such as dissolution-precipitation creep may promote weakening at both low and high strains, or iii) a combination of multiple deformation mechanisms are active that aid in muscovite aligning sub-parallel to the shear plane.

While dissolution precipitation creep likely plays an important role in the redistribution and interconnection of muscovite with increasing strain, several observations suggest basal slip remains the rheologically-controlling mechanism in our samples. First, in the high strain samples, neocrystallized muscovite grains are common but not ubiquitous throughout all the muscovite-bearing samples. If dissolution-precipitation creep were the dominant deformation mechanism throughout the muscovite-bearing samples, one might expect more prevalent precipitation of muscovite into the fluid-filled spaces as shown in Fig. 9a, but this is not commonly observed. Second, if dissolution precipitation had been the dominant deformation mechanism, one might also expect to see widespread neocrystallizion of muscovite in the low strain samples, but this is not observed. Third, the observation that quartz-muscovite samples deformed in axial compression (Tullis and Wenk, 1994) show less weakening than our general shear experiments for a given volume percent of muscovite (Fig. 18), suggests muscovite grain orientation is important to the strength of mica-bearing samples. In contrast, if solution-precipitation creep were the dominant deformation mechanism we'd expect a similar weakening effect regardless of deformation geometry. Fourth, the diffusion length scale (e.g. the relict quartz grain size) is likely too large to allow for dissolution-precipitation creep to be the dominant mechanism throughout the aggregate over the duration of these experiments. However, as outlined in the next section, dissolution-precipitation creep is important to mechanical and microstructural evolution through the formation of C′ bands in our mica-bearing aggregates.

4.4. Muscovite and quartz C′-bands

The development and evolution of C′-bands, Ms C′-bands, and the localization of fluids through the development of these bands can lead to local and/or global interconnection of weak layer networks with increasing strain. We propose that the connection of C′-bands with muscovite grains promotes increased interconnection of weak layers within the aggregate. Fig. 19 (see also Fig. 13) shows phase maps for the high strain muscovite-bearing samples with and without C′-bands highlighted. Without the C′-bands, through-going layers of muscovite are not observed in the 5% muscovite sample, however, with C′-bands
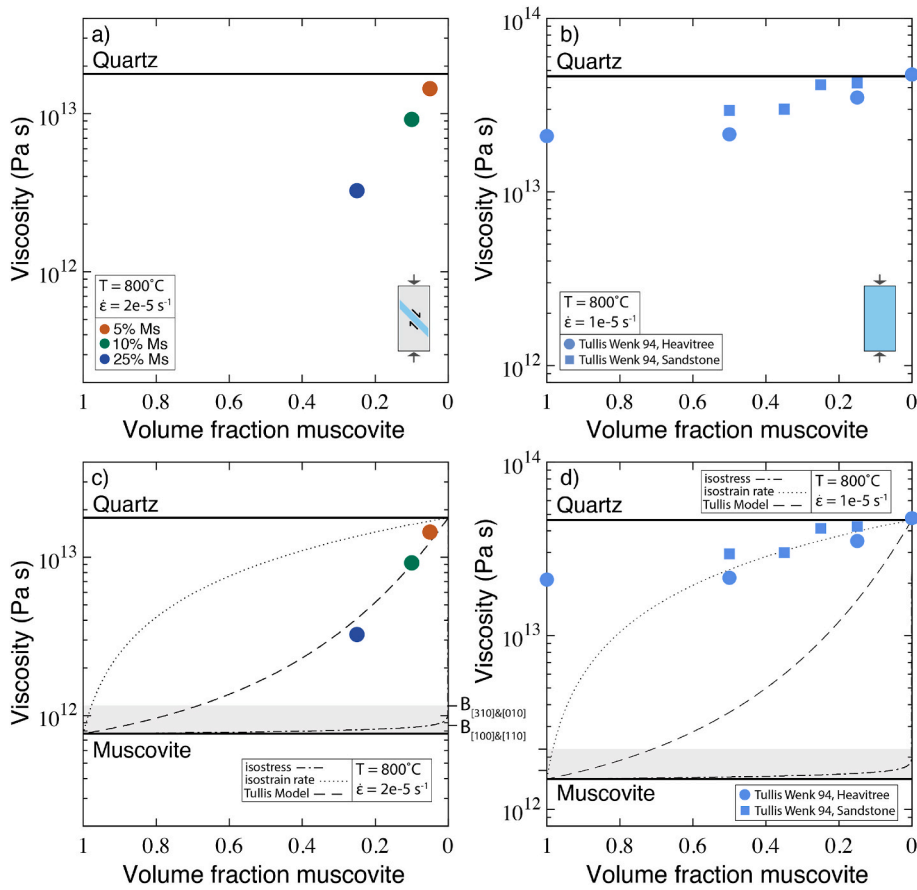
Fig. 18. Plots of log viscosity versus volume fraction of muscovite for a) the high strain samples and b) axial compression experiments on 'as-is' quartz-muscovite aggregates from Tullis and Wenk (1994). c,d) Plots of log viscosity versus volume fraction of muscovite comparing the viscosity of the c) high strain muscovite-bearing aggregates and d) the Tullis and Wenk (1994) aggregates to the isostress, isostrain rate, and Tullis et al. (1991) rheological mixing models. For a,c) the water fugacity is 4840 MPa while in b,d) the water fugacity used for the flow law was lowered from 4840 to 1100 MPa to account for the lower water content of the as-is samples, and match the observed viscosity of the pure. In all plots, the thick black horizontal lines represent the quartz and muscovite viscosities based on the $n = 3$ flow law by Tokle et al. (2019) and a power law flow law derived based on the mechanical data from Mares and Kronenberg (1993), see text for flow law details. In c,d), the grey regions represents the biotite single crystal flow laws for easy and hard slip orientations derived from Kronenberg et al. (1990). In the bottom right side of a,b) cartoons of the deformation geometries are shown to illustrate a) the general shear geometry and b) the axial compression geometry with the vertical arrows representing the axial shortening direction. The y-axis is scaled to the same range (2.2 orders of magnitude) in all plots for direct comparison.
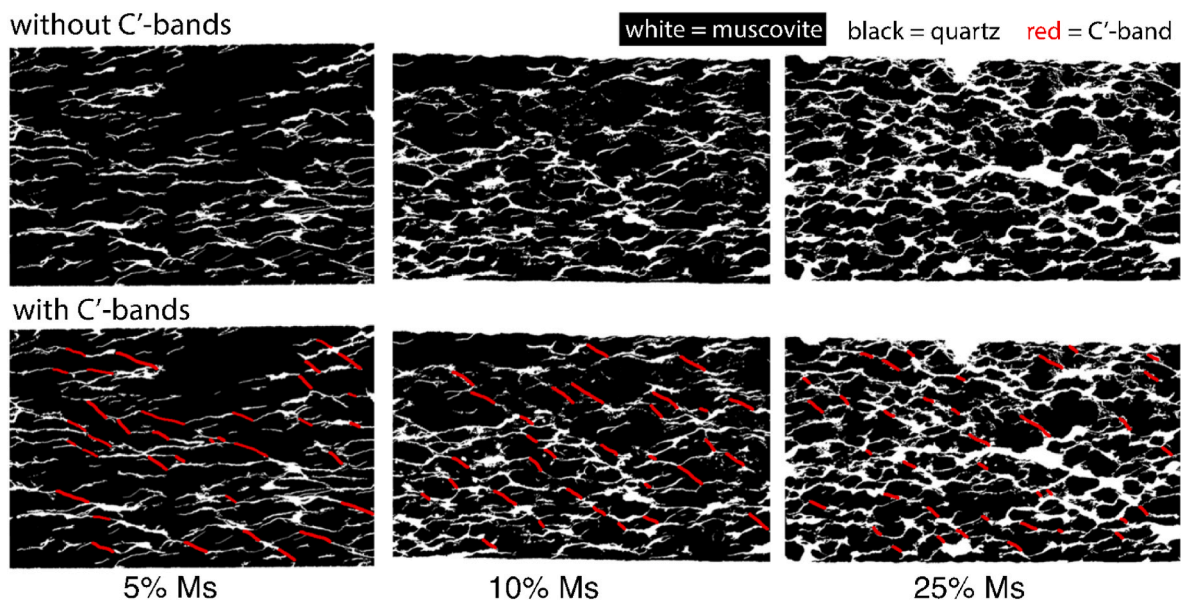
Fig. 19. Phase maps of the high strain muscovite-bearing samples. White regions represent muscovite and black regions represent quartz. The shear plane for each map is parallel to the horizontal plane of the image with a dextral sense of shear. Red lines are drawn in to show the location of C'-bands. (For interpretation of the references to color in this figure legend, the reader is referred to the Web version of this article.)

drawn in, the isolated muscovite grains become more interconnected. In the 10% muscovite sample, muscovite grains are less isolated where C'-bands and Ms C'-bands develop, and together, the mica and the C'-bands create a more interconnected network in 2D (Fig. 19). In the 25% muscovite sample, muscovite already forms an interconnected network

in 2D, however C'-bands are still observed at quartz grain boundaries creating an even more interconnected network of C'-bands and Ms C'-bands (Fig. 19).

C'-bands observed in other experimental studies have been interpreted to promote weakening. Holyoke and Tullis (2006a) observed

C′-band microstructures in their low phase strength contrast (PSC) general shear experiments on mica-rich gneiss. In their high PSC experiments, Holyoke and Tullis (2006a) observed small-scale faults emanating from biotite grains that lead to through-going weak zones. Similar C′-band structures have been observed in other experimental studies, including quartz-iron oxide (Gonçalves et al., 2014) and plagioclase (Stünitz and Tullis, 2001) aggregates; in these studies, the C′-bands are defined by fine-grained reaction products, which were inferred to promote weakening. Additionally, numerical studies have also shown that the development of C′-bands promote weakening in mica-bearing aggregates (Johnson et al., 2004; Finch et al., 2020; Rast and Ruh, 2021).

Fluid-filled pores aligned within C′-bands highlight the presence and redistribution of fluids into low stress orientations with increasing strain. Similar pore networks are preserved in experimentally deformed partially molten dunite (Holtzman et al., 2003), fluid-rich quartzite (Palazzin et al., 2018; Okazaki et al., 2021), and inferred from microstructures in naturally deformed quartz-rich rocks (Hippertt, 1994; Mancktelow et al., 1998; Geraud et al., 1995; Fusseis et al., 2009). In addition, C′-bands promote phase mixing which can lead to a switch from grain size insensitive to grain size sensitive deformation mechanisms (Kilian et al., 2011a). With smaller grains and localization of fluids enhancing diffusion in the both the C′-bands and parallel to the foliation plane, grain size sensitive creep may play an important role in the microstructural evolution of mica-bearing aggregates.

4.5. Muscovite stability

The presence of neocrystallized muscovite through dissolution and precipitation is the best evidence highlighting the stability of muscovite in our samples (Fig. 9 and Supplementary Fig. S4). Extrapolation of the $Qz + Ms + H_2O$ stability fields developed by Rubie and Brearley (1987)

and Vielzeuf and Holloway (1988) shows that our samples are near the conditions where break down occurs to form aluminosilicate + melt; while stability fields for H_2O undersaturated conditions indicate muscovite is stable at our deformation conditions (Rubie and Brearley, 1987; Vielzeuf and Holloway, 1988). The kinetics for these reactions at 1.0 GPa are very slow relative to the duration of our deformation experiments. Given the presence of reaction products in all of the muscovite-bearing samples, partial dehydroxylation of muscovite cannot be entirely ruled out. As noted by Mariani et al. (2006), as OH are lost during muscovite dehydroxylation, the remaining Al–OH bonds are strengthened inhibiting further dehydroxylation, which suggests that partial dehydroxylation in muscovite may have occurred in our samples, but reached a stable equilibrium. Based on these observations, we are confident that muscovite is stable throughout our experiments and the reaction products have little to no effect on our mechanical or microstructural analyses.

4.6. Implications for crustal rheology

To provide a first order estimate of the effect of muscovite on quartz rheology we plot stress versus depth plots as well as plots showing the increase in strain rate for a given temperature and stress for aggregates with 5, 10, and 25% muscovite using the Tullis et al. (1991) mixing law with the muscovite power law flow law and the $n = 3$ and $n = 4$ quartz flow laws from Tokle et al. (2019) (Fig. 20). At depths greater than approximately 15–20 km, the extrapolation of the flow laws suggests that muscovite is the more viscous phase (owing to the high stress exponent and low activation enthalpy for the muscovite flow law). This observation is nominally supported by deformation microstructures, such as biotite micro-boudins in a granitic protomylonite (see Fig. 7d in Gottardi et al., 2020). However, as outlined in section 4.3, the possibility that the presence of mica promotes dissolution-precipitation creep at
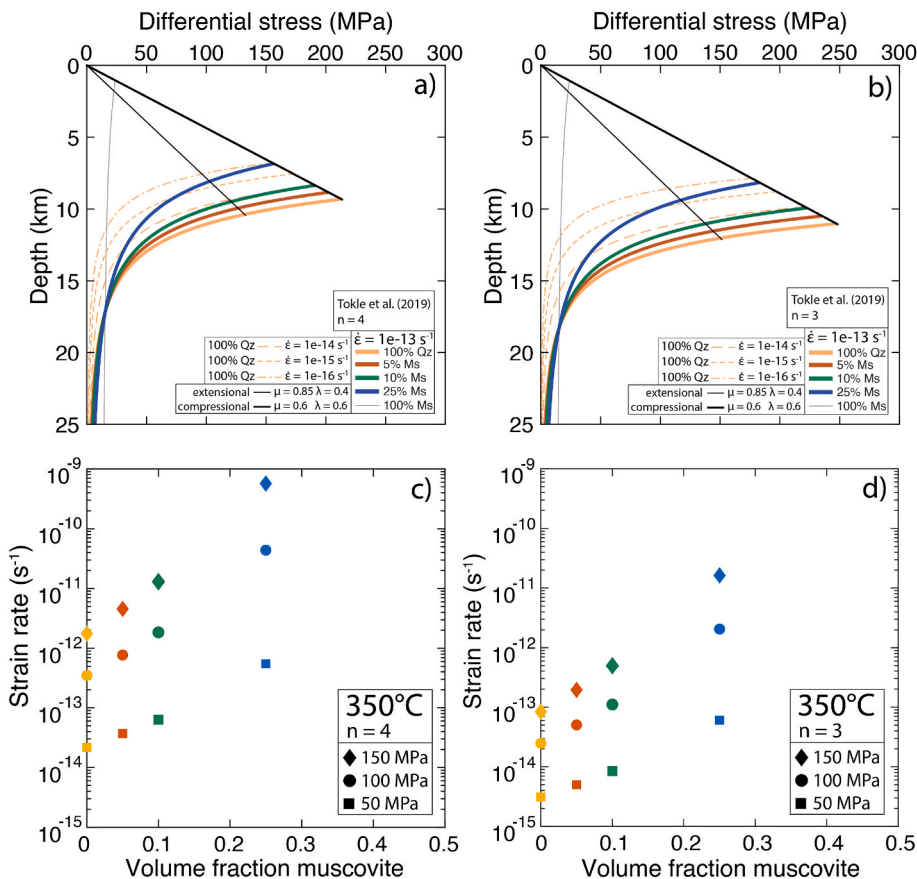

Fig. 20. Plots of stress versus depth and volume fraction of muscovite versus strain rate estimating the effect of muscovite on the quartz-muscovite aggregate rheology. The stress versus depth plots a,b) and the strain rates in c,d) are calculated using the Tullis et al. (1991) mixing law with the a,c) $n = 4$ and b,d) $n = 3$ extrapolated quartz flow laws from Tokle et al. (2019) and the muscovite power law flow law (see Fig. 15–17). In a,b) the thermal gradient is 30 °C/km. The thin black line is the frictional stress assuming a vertical maximum principal stress defined by equation 7a in Zoback and Townend (2001) with μ = 0.85 and a ratio of pore fluid pressure to lithostatic pressure of λ = 0.4, following Behr and Platt (2011). The thick black line is the frictional stress assuming a horizontal maximum principal stress defined by equation 7c in Zoback and Townend (2001) with μ = 0.6 and λ = 0.6 following Tokle and Hirth (2021).

higher pressure and temperature conditions must be acknowledged. At more shallow depths our results indicate an aggregate with 25% muscovite has a strength ~25% lower than 100% quartz for a strain rate of 10^{-13} s^{-1} near the brittle-viscous transition (Fig. 20a and b). Similarly, for a given stress, the muscovite-bearing aggregates are predicted to deform at a faster strain rate (Fig. 20c and d). For example, at 100 MPa a 100% quartz aggregate is predicted to deform approximately two orders of magnitude slower than an aggregate with 25% muscovite (Fig. 20c and d). This effect becomes less significant with increasing temperature/depth or decreasing stress based on the muscovite power law flow law; however, with decreasing stress the muscovite power law flow law likely overestimates muscovite strength suggesting muscovite may still significantly weaken quartz-muscovite aggregates at low stress conditions (Fig. 16).

Lusk et al. (2021) developed a dislocation creep flow law for quartz that predicts strain rates approximately one order of magnitude faster than existing dislocation creep flow laws at geologic conditions; however, their faster flow law can be explained by the rheological influence of micas on quartz rheology. They use a combination of deformation experiments and estimates from naturally deformed quartz-rich rocks to constrain a dislocation creep flow law in quartz. The naturally deformed rocks used in their analysis come from shear zones in northwest Scotland where the shear zones are estimated to range from several kilometers to ~100 m in thickness over a range of mid-crustal temperature and pressure conditions (Lusk and Platt, 2020). Mineralogically, the shear zones primarily contain quartz, mica, and feldspar where quartz largely deforms by dislocation creep, however evidence for pressure solution creep in fine-grained quartz-mica layers is observed (Lusk and Platt, 2020). At all deformation conditions micas or mica-rich layers define the foliation of the shear zone and are the weakest phase at all conditions where there is no overprinted annealing (see Fig. 7 in Lusk and Platt, 2020). We also highlight the microstructural similarity between our high strain muscovite-bearing samples and the micaceous quartzite from domain 2a characterized by Lusk and Platt (2020) (see Fig. 8a in Lusk and Platt, 2020). Strain rates for these shear zones were determined based on the estimated minimum displacement rate across the shear zone width; therefore, the strain rate estimates represent deformation accommodated by all phases (quartz, micas, and feldspar) and deformation mechanisms (dislocation creep, basal glide, pressure solution, etc). Lusk et al. (2021) assume in their analysis that these strain rates represent dislocation creep in quartz while also highlighting that their strain rate estimates are significantly faster than predicted from existing dislocation creep flow laws for quartzite (see Fig. 10 in Lusk et al., 2021). We suggest the presence of mica in their samples could account for this apparent discrepancy. As shown in Fig. 20c and d, accounting for the influence of 10–25% mica (in the range of what is apparent in the micrographs presented in Lusk and Platt, 2020), strain rates at natural conditions can be enhanced by approximately an order of magnitude or more relative to pure quartz aggregates. While quartz is one of the most important minerals defining the rheology of the middle crust, the influence of micas on crust rheology should not be ignored.

5. Conclusions

General shear experiments were conducted on synthetic mixtures of quartz and muscovite aggregates at 1.5 GPa, 800 °C, and shear strain rates ~2×10^{-5} s^{-1} with 0.1 wt% water added. The volume percent of muscovite ranged from 0% to 25% and was homogeneously mixed with quartz. The mechanical data shows that as the volume percent of muscovite increases the aggregate strength decreases with the high strain pure quartz sample ~4 times stronger than the 25% muscovite sample. The presence of muscovite had a significant effect on the microstructural evolution of quartz:

- The volume percent of dynamically recrystallized quartz decreased substantially as the volume percent of muscovite increased, from

nearly complete recrystallization in the pure quartz sample to ~5% recrystallization in the 25% muscovite sample.
- The fabric strength of the high strain quartz CPO decreases with increasing muscovite content. The orientation of quartz CPO also varies with muscovite content, with the pure quartz c-axes aligning approximately normal to the shear plane while the c-axes in the 25% muscovite sample are approximately parallel to the axial shortening direction.
- At high strains, muscovite largely aligned in the C-plane, however, all muscovite-bearing samples develop rheologically weak layers in the C′-planes, either through the connection of muscovite grains (Ms C′-bands) or through localized quartz recrystallization (C′-bands).

Author statement

All authors listed on this manuscript contributed to its production. L. T. conducted the deformation experiments, microstructural analyses, and rheological calculations as well as wrote the initial manuscript draft. All authors contributed to the conception of the paper. G.H. and H.S. assisted in interpreting microstructural and mechanical data, and contributed to editing the manuscript.

Declaration of competing interest

The authors declare that they have no known competing financial interests or personal relationships that could have appeared to influence the work reported in this paper.

Data availability

Data used in this study are available through the ETH Research Collection (https://doi.org/10.3929/ethz-b-000603035).

Appendix A. Supplementary data

Supplementary data to this article can be found online at https://doi.org/10.1016/j.jsg.2023.104835.

References

Aslin, J., Mariani, E., Dawson, K., Barsoum, M.W., 2019. Ripplocations provide a new mechanism for the deformation of phyllosilicates in the lithosphere. Nat. Commun. 10, 686. https://doi.org/10.1038/s41467-019-08587-2.

Behr, W.M., Platt, J.P., 2011. A naturally constrained stress profile through the middle crust in an extensional terrane. Earth Planet Sci. Lett. 303, 181–192. https://doi.org/10.1016/j.epsl.2010.11.044.

Bell, T.H., Cuff, C., 1989. Dissolution, solution transfer, diffusion versus fluid flow and volume loss during deformation/metamorphism. J. Metamorphic Geol. 7, 425–447.

Bell, I.A., Wilson, C.J.L., McLaren, A.C., Etheridge, M.A., 1986. Kinks in mica: role of dislocations and (001) cleavage. Tectonophysics 127, 49–65.

Bons, P.D., Urai, J.L., 1994. Experimental deformation of two-phase rock analogues. Mater. Sci. Eng. A175, 221–229.

Brearley, A.J., Rubie, D.C., 1990. Effects of H_2O on the disequilibrium breakdown of muscovite + quartz. J. Petrol. 31 (4), 925–956.

Burdette, E., Hirth, G., 2022. Creep rheology of antigorite: experiments at subduction zone conditions. J. Geophys. Res. 127, e2022JB024260 https://doi.org/10.1029/2022JB024260.

de Ronde, A.A., Stünitz, H., Tullis, J., Heilbronner, R., 2005. Reaction-induced weakening of plagioclase-olivine composites. Tectonophysics 409, 85–108.

Derez, T., Pennock, G., Drury, M., Sintubin, M., 2015. Low-temperature intracrystalline deformation microstructures in quartz. J. Struct. Geol. 71, 3–23.

Dimanov, A., Dresen, G., 2005. Rheology of synthetic anorthite-diopside aggregates: implications for ductile shear zones. J. Geophys. Res. 110, B07203 https://doi.org/10.1029/2004JB003431.

Farver, J.R., Yund, R.A., 1999. Oxygen bulk diffusion measurements and TEM characterization of a natural ultramylonite: implications for fluis transport in mica-bearing rocks. J. Metamorph. Petrol. 17, 669–683.

Finch, M.A., Bons, P.D., Steinbach, F., Griera, A., Llorens, M.-G., Gomez-Rivas, E., Ran, H., de Riese, T., 2020. The ephemeral development of C' shear bands: a numerical modelling approach. J. Struct. Geol. 139, 104091.

Fischer, G.J., Paterson, M.S., 1992. Measurements of permeability and storage capacity in rocks during deformation at high temperatures and pressure. In: Evans, B., Wong, T.F. (Eds.), Fault Mechanics and Transport Properties of Rocks. Elsevier, New York, pp. 213–252.

Frost, H.J., Ashby, M.F., 1982. Deformation Mechanism Maps: the Plasticity and Creep of Metals and Ceramics. Pergamon press.

Fusseis, F., Regenauer-Lieb, K., Liu, J., Hough, R.M., De Carlo, F., 2009. Creep cavitation can establish a dynamic granular fluid pump in ductile shear zones. Nature 459. https://doi.org/10.1038/nature08051.

Geraud, Y., Caron, J.-M., Faure, P., 1995. Porosity network of a ductile shear zone. J. Struct. Geol. 17, 1757–1769. https://doi.org/10.1016/0191-8141(95)00067-N.

Gonçalves, C.C., Gonçalves, L., Hirth, G., 2014. The effect of quartz recrystallization and reaction on weak phase interconnection, strain localization and evolution of microstructure. J. Struct. Geol. 71, 1–17.

Gottardi, R., McAleer, R., Casale, G., Borel, M., Iriondo, A., Jepson, G., 2020. Exhumation of the Coyote Mountains Metamorphic Core Complex (Arizona): Implications for Orogenic Collapse of the Southern North American Cordillera. https://doi.org/10.1029/2019TC006050.

Gottschalk, R.R., Kronenberg, A.K., Russell, J.E., Handin, J., 1990. Mechanical anisotropy of gneiss; failure criterion and textural sources of directional behavior. J. Geophys. Res. 95, 21,613 – 21,634.

Guggenheim, S., Chang, Y.-H., Koster van Groos, A.F., 1987. Muscovite dihydroxylation: high-temperature studies. Am. Mineral. 72, 537–550.

Handy, M.R., 1990. The solid-state flow of polymineralic rocks. J. Geophys. Res. 95, 8647–8661.

Handy, M.R., 1994. Flow laws for rocks containing two non-linear viscous phases: a phenomenological approach. J. Struct. Geol. 16, 287–301.

Heilbronner, R., Tullis, J., 2006. Evolution of c axis pole figures and grain size during dynamic recrystallization: results from experimentally sheared quartzite. J. Geophys. Res. 111 https://doi.org/10.1029/2005JB004194.

Hippertt, J.F.M., 1994. Grain boundary microstructures in micaceous quartzite: significance for fluid movement and deformation processes in low metamorphic grade shear zones. J. Geol. 102, 331–348.

Hirth, G., Teyssier, C., Dunlap, W.J., 2001. An evaluation of quartzite flow laws based on comparisons between experimentally and naturally deformed rocks. Int. J. Earth Sci. 90, 77–87. https://doi.org/10.1007/s005310000152.

Holtzman, B.K., Groebner, N.J., Zimmerman, M.E., Ginsberg, S.B., Kohlstedt, D.L., 2003. Stress-driven melt segregation in partially molten rocks. Geochem. Geophys. Geosys. 4 https://doi.org/10.1029/2001GC000258.

Holyoke, C.W., Kronenberg, A.K., 2010. Accurate differential stress measurements using the molten salt cell and solid salt assemblies in the Griggs apparatus with applications to strength, piezometers and rheology. Tectonophysics 494, 18–31.

Holyoke, C.W., Tullis, J., 2006a. Mechanisms of weak phase interconnection and the effects of phase strength contrast on fabric development. J. Struct. Geol. 28, 621–640. https://doi.org/10.1016/j.jsg.2006.01.008.

Holyoke, C.W., Tullis, J., 2006b. Formation and maintenance of shear zones. Geology 34, 105–108. https://doi.org/10.1130/G22116.1.

Holyoke, C.W., Tullis, J., 2006c. The interaction between reaction and deformation: an experimental study using a biotite + plagioclase + quartz gneiss. J. metamorphic Geol. 24, 743–762.

Huet, B., Yamato, P., Grasemann, B., 2014. The minimized power geometric model: an analytical mixing model for calculating polyphase rock viscosities consistent with experimental data. J. Geophys. Res. Solid Earth 119. https://doi.org/10.1002/2013JB010453.

Hunter, N.J.R., Hasalová, P., Weinberg, R.F., Wilson, C.J.L., 2016. Fabric controls on strain accommodation in naturally deformed mylonites: the influence of interconnected micaceous layers. J. Struct. Geol. 83, 180–193.

Hunter, N.J.R., Weinberg, R.F., Wilson, C.J.L., Luzin, V., Misra, S., 2019. Quartz deformation across interlayered monomineralic and polymineralic rocks: a comparative analysis. J. Struct. Geol. 119, 118–134.

Johnson, S.E., Vernon, R.H., Upton, P., 2004. Foliation development and progressive strain-rate partitioning in the crystallizing carapace of a tonalite pluton: microstructural evidence and numerical modeling. J. Struct. Geol. 26, 1845–1865.

Jordan, P.G., 1987. The deformation behavior of bimineralic limestone-halite aggregates. Tectonophysics 135, 185–197.

Kilian, R., Heilbronner, R., Stunitz, H., 2011a. Quartz grain size reduction in a granitoid rock and the transition from dislocation to diffusion creep. J. Struct. Geol. 33, 1265–1284. https://doi.org/10.1016/j.jsg.2011.05.004.

Kilian, R., Heilbronner, R., Stünitz, H., 2011b. Quartz microstructures and crystallographic preferred orientation: which shear sense do they indicate? J. Struct. Geol. 33, 1446–1466.

Krabbendam, M., Urai, J.L., van Vliet, L.J., 2003. Grain size stabilization by dispersed graphite in a high-grade quartz mylonite: an example from Naxos (Greece). J. Struct. Geol. 25, 855–866.

Kronenberg, A.K., Kirby, S.H., Pinkston, J., 1990. Basal slip and mechanical anisotropy of biotite. J. Geophys. Res. 95, 19257–19278.

Lister, G.S., Hobbs, B.E., 1980. The simulation of fabric development during plastic deformation and its application to quartzite: the influence of deformation history. J. Struct. Geol. 2, 355–370.

Lister, G.S., Paterson, M.S., Hobbs, B.E., 1978. Simulation of fabric development during plastic deformation and its application to quartzite: model. Tectonophysics 45, 107–158.

Little, T.A., Prior, D.J., Toy, V.G., Lindroos, Z.R., 2015. The link between strength of lattice preferred orientation, second phase content and grain boundary migration: a case study from the Alpine Fault zone, New Zealand. J. Struct. Geol. 81, 59–77.

Lusk, A.D.J., Platt, J.P., 2020. The deep structure and rheology of a plate boundary-scale shear zone: constraints from an exhumed caledonian shear zone, NW Scotland. Lithosphere 1–33. https://doi.org/10.2113/2020/8824736.

Lusk, A.D.J., Platt, J.P. Platt, Platt, J.A., 2021. Natural and experimental constraints on a flow law for dislocation-dominated creep in wet quartz. J. Geophys. Res. Solid Earth 126, e2020JB021302.

Mancktelow, N.S., Grujic, D., Johnson, E.L., 1998. An SEM study of porosity and grain boundary microstructure in quartz mylonites, Simplon Fault Zone, Central Alps. Contrib. Mineral. Petrol. 131, 71–85.

Manning, C., 2018. Fluids of the lower crust: deep is different. Annu. Rev. Earth Planet Sci. 46, 67–97.

Mares, V.M., Kronenberg, A.K., 1993. Experimental deformation of muscovite. J. Struct. Geol. 15, 1061–1075.

Mariani, E., Brodie, K.H., Rutter, E.H., 2006. Experimental deformation of muscovite shear zones at high temperatures under hydrothermal conditions and the strength of phyllosilicate-bearing faults in nature. J. Struct. Geol. 28, 1569–1587. https://doi.org/10.1016/j.jsg.2006.06.009.

Mazzucato, E., Artioli, G., Gualtieri, A., 1999. High temperature dihydroxylation of muscovite-2M$_1$: a kinetic study by in situ XRPD. Phys. Chem. Miner. 26, 375–381.

Meike, A., 1989. In situ deformation of micas; a high-voltage electron-microscope study. Am. Mineral. 74, 780–796.

Morales, L.F.G., Mainprice, D., Lloyd, G., Law, R.D., 2011. Crystal fabric development and slip systems in a quartz mylonite: an approach via transmission electron microscopy and viscoplastic self-consistent modelling, 360. Geol. Soc., London, pp. 151–174 (From: Prior, D.J., Rutter, E.H., and Tatham, D.J., Deformation Mechanisms, Rheology, and Tectonics: Microstructures, Mechanics and Anisotropy).

Mulch, A., Teyssier, C., Cosca, M.A., Vennemann, T.W., 2006. Thermomechanical analysis of strain localization in a ductile detachment zone. J. Geophys. Res. 111, B12405 https://doi.org/10.1029/2005JB004032.

Muto, J., Hirth, G., Heilbronner, R., Tullis, J., 2011. Plastic anisotropy and fabric evolution in sheared and recrystallized quartz single crystals. J. Geophys. Res. 116 https://doi.org/10.1029/2010JB007891.

Okazaki, K., Burdette, E., Hirth, G., 2021. Rheology of the fluid oversaturated fault zones at the Brittle-Plastic transition. JGR-SE 126 (2), e2020JB020804.

Palazzin, G., Raimbourg, H., Stünitz, H., Heilbronner, R., Neufeld, K., Précigout, J., 2018. Evolution in H$_2$O contents during deformation of polycrystalline quartz: an experimental study. J. Struct. Geol. 114, 95–110.

Panozzo, R., 1984. Two-dimensional strain from the orientation of lines in a plane. J. Struct. Geol. 6, 215–221.

Panozzo Heilbronner, R., Pauli, C., 1993. Integrated spatial and orientation analysis of quartz c-axes by computer-aided microscopy. J. Struct. Geol. 15, 369–382.

Paterson, M.S., Olgaard, D.L., 2000. Rock deformation tests to large shear strains in torsion. J. Struct. Geol. 22, 1341–1358. https://doi.org/10.1016/S0191-8141(00)00042-0.

Pec, M., Stünitz, H., Heilbronner, R., Drury, M., de Capitani, C., 2012. Origin of pseudotachylites in slow creep experiments. Earth Planet Sci. Lett. 355–356, 299–310.

Pitzer, K.S., Sterner, S.M., 1994. Equation of state valid continuously from zero to extreme pressures for H$_2$O and CO$_2$. J. Chem. Phys. 101, 3111–3116.

Rast, M., Ruh, J.B., 2021. Numerical shear experiments of quartz-biotite aggregates: insights on strain weakening and two-phase flow laws. J. Stuct. Geol. 149, 104375 https://doi.org/10.1016/j.jsg.2021.104375.

Rawling, G.C., Baud, P., Wong, T., 2002. Dilatancy, brittle strength, and anisotropy of foliated rocks: experimental deformation and micromechanical modeling. J. Geophys. Res. 107, 2234. https://doi.org/10.1029/2001JB000472. B10.

Richter, B., Stünitz, H., Heilbronner, R., 2018. The brittle-to-viscous transition in polycrystalline quartz: an experimental study. J. Struct. Geol. 114, 1–21. https://doi.org/10.1016/j.jsg.2018.06.005.

Rubie, D., Brearley, A.J., 1987. Metastable melting during the breakdown of muscovite + quartz at 1 kbar. Bull. Mineral. 110, 533–549.

Shea, W.T., Kronenberg, A.K., 1992. Rheology and deformation mechanisms of an isotropic mica schist. J. Geophys. Res. 97, 15201–15237.

Shea, W.T., Kronenberg, A.K., 1993. Strength and anisotropy of foliated rocks with varied mica contents. J. Struct. Geol. 15, 1097–1121.

Shimizu, I., 1995. Kinetics of pressure solution creep in quartz: theoretical considerations. Tectonophysics 245, 121–134.

Song, W.T., Ree, J.H., 2007. Effect of mica on the grain size of dynamically recrystallized quartz in a quartz-muscovite mylonite. J. Struct. Geol. 29, 1872–1881.

Stünitz, H., Tullis, J., 2001. Weakening and strain localization produced by syn-deformational reaction of plagioclase. Int. J. Earth Science (Geol Rundsch) 90, 136–148.

Stünitz, H., Thrust, A., Heilbronner, R., Behrens, H., Kilian, R., Tarantola, A., Fitz Gerald, J.D., 2017. Water redistribution in experimentally deformed natural milky quartz single crystals – implications for H2O-weakening processes. J. Geophys. Solid Earth 122, 866–894.

Thompson, A.B., Connolly, J.A.D., 1990. Metamorphic fluids and anomalous porosities in the lower crust. Tectonophysics 182, 47–55.

Tokle, L., Hirth, G., 2021. Assessment of quartz grain growth and the application of the wattmeter to predict quartz recrystallized grain sizes. JGR – Solid Earth 126, e2020JB021475.

Tokle, L., Hirth, G., Behr, W.M., 2019. Flow law and fabric transition in wet quartzite. Earth Planet Sci. Lett. 505, 152–161.

Tullis, J., Wenk, H.-R., 1994. Effect of muscovite on the strength and lattice preferred orientations of experimentally deformed quartz aggregates. Mater. Sci. Eng. A175, 209–220.

Tullis, J., Christie, J.M., Griggs, D.T., 1973. Microstructures and preferred orientations of experimentally deformed quartzites. Bull. Geol. Soc. Am. 84, 297–314.

Tullis, T.E., Horowitz, F.G., Tullis, J., 1991. Flow laws of polyphase aggregates from end-member flow laws. J. Geophys. Res. 96, 8081–8096.

Vielzeuf, D., Holloway, J.R., 1988. Experimental determination of the fluid-absent melting relations in the pelitic system. Contrib. Mineral. Petrol. 98, 257–276.

Wintsch, R.P., Yi, K., 2002. Dissolution and replacement creep: a significant deformation mechanism in mid-crustal rocks. J. Struct. Geol. 24, 1179–1193.

Wintsch, R.P., Christoffersen, R., Kronenberg, A.K., 1995. Fluid-rock reaction weakening of fault zones. J. Geophys. Res. 100, 13021–13032.

Zhang, S., Cox, S.F., Paterson, M.S., 1994. The influence of room temperature deformation on porosity and permeability in calcite aggregate. J. Geophys. Res. 99, 15,761-15,775.

Zoback, M., Townend, J., 2001. Implications of hydrostatic pore pressures and high crustal strength for the deformation of intraplate lithosphere. Tectonophysics 336, 19–30. https://doi.org/10.1016/s0040-1951(01)00091-9.